

A non-interacting Galactic black hole candidate in a binary system with a main-sequence star

SUKANYA CHAKRABARTI,¹ JOSHUA D. SIMON,² PETER A. CRAIG,³ HENRIQUE REGGIANI,² TIMOTHY D. BRANDT,⁴
PURAGRA GUHATHAKURTA,⁵ PAUL A. DALBA,^{6,7,8} EVAN N. KIRBY,⁹ PHILIP CHANG,¹⁰ DANIEL R. HEY,¹¹
ALESSANDRO SAVINO,¹² MARLA GEHA,¹³ AND IAN B. THOMPSON²

¹*Department of Physics and Astronomy, University of Alabama, Huntsville, 301 North Sparkman Drive, Huntsville, USA*

²*Observatories of the Carnegie Institution for Science, 813 Santa Barbara St., Pasadena, CA 91101, USA*

³*School of Physics and Astronomy, Rochester Institute of Technology, 1 Lomb Memorial Dr, Rochester, NY 14623*

⁴*Department of Physics, University of California, Santa Barbara, Santa Barbara, CA 93106, USA*

⁵*University of California Santa Cruz, UCO/Lick Observatory, 1156 High St., Santa Cruz, CA 95064, USA*

⁶*Heising-Simons 51 Pegasi b Postdoctoral Fellow*

⁷*Department of Astronomy and Astrophysics, University of California, Santa Cruz, CA 95064, USA*

⁸*SETI Institute, Carl Sagan Center, 339 Bernardo Ave, Suite 200, Mountain View, CA 94043, USA*

⁹*Department of Physics and Astronomy, University of Notre Dame, 225 Nieuwland Science Hall, Notre Dame, IN 46556, USA*

¹⁰*Department of Physics, University of Wisconsin-Milwaukee, 3135 North Maryland Avenue, Milwaukee, WI 53211, USA*

¹¹*Institute for Astronomy, University of Hawai'i, Honolulu, HI 96822, USA*

¹²*Department of Astronomy, University of California, Berkeley, Berkeley, CA, 94720, USA*

¹³*Department of Astronomy, Yale University, 52 Hillhouse Avenue, New Haven, CT 06520, USA*

ABSTRACT

We describe the discovery of a solar neighborhood ($d = 468$ pc) binary system with a main-sequence sunlike star and a massive non-interacting black hole candidate. The spectral energy distribution (SED) of the visible star is described by a single stellar model. We derive stellar parameters from a high signal-to-noise Magellan/MIKE spectrum, classifying the star as a main-sequence star with $T_{\text{eff}} = 5972\text{K}$, $\log g = 4.54$, and $M = 0.91 M_{\odot}$. The spectrum shows no indication of a second luminous component. To determine the spectroscopic orbit of the binary, we measured radial velocities of this system with the Automated Planet Finder, Magellan, and Keck over four months. We show that the velocity data are consistent with the *Gaia* astrometric orbit and provide independent evidence for a massive dark companion. From a combined fit of our spectroscopic data and the astrometry, we derive a companion mass of $11.39^{+1.51}_{-1.31} M_{\odot}$. We conclude that this binary system harbors a massive black hole on an eccentric ($e = 0.46 \pm 0.02$), 185.4 ± 0.1 d orbit. These conclusions are independent of [El-Badry et al. \(2023a\)](#), who recently reported the discovery of the same system. A joint fit to all available data (including [El-Badry et al. \(2023a\)](#)'s) yields a comparable period solution, but a lower companion mass of $9.32^{+0.22}_{-0.21} M_{\odot}$. Radial velocity fits to all available data produce a unimodal solution for the period that is not possible with either data set alone. The combination of both data sets yields the most accurate orbit currently available.

1. INTRODUCTION

Simple stellar population calculations suggest that stellar mass black holes should be abundant (e.g., [Breivik et al. 2017](#); [Wiktorowicz et al. 2019](#)), with $\sim 10^8$ present in the Milky Way (e.g., [Olejak et al. 2020](#)). However, black holes in this mass range are difficult to identify observationally. Isolated black holes can only be detected with gravitational microlensing (e.g., [Lam et al. 2022](#); [Sahu et al. 2022](#)), while black holes in binary systems are easily detectable only when the companion star is close enough for an accretion disk to form. Although dozens of X-ray binaries with black hole candidates in short-period orbits have been identified (e.g.,

[Corral-Santana et al. 2013, 2016](#); [Panizo-Espinar et al. 2022](#); [Russell et al. 2022](#)), wider binaries have proven challenging to find.

The detection of gravitational waves from black hole merger events with LIGO (e.g., [Abbott et al. 2016, 2019, 2021](#)) provided a new avenue for discovering binary black holes beyond the X-ray bright population ([Corral-Santana et al. 2016](#)). However, like the X-ray binaries, LIGO black hole mergers are necessarily found in very tight orbits. With the publication of the large catalog of binary systems included in the third *Gaia* data release (DR3; [Gaia Collaboration et al. 2016, 2022a](#); [Halbwachs et al. 2022](#); [Gaia Collaboration et al. 2022b](#)) and the an-

ticipated even larger data set to come in DR4, we can expect to significantly expand upon discoveries of black holes in binary systems, and particularly for black holes in long-period systems that can be characterized by measuring accelerations from astrometric and spectroscopic data (e.g., Breivik et al. 2017; Mashian & Loeb 2017; Yamaguchi et al. 2018; Wiktorowicz et al. 2020; Chawla et al. 2022; Janssens et al. 2022). Since binaries are co-eval, studying these systems may help in understanding the dependence of the formation rate of black holes in binaries on metallicity and age, and thereby indirectly on the formation channel.

Several mechanisms for the formation of black holes in binary systems have been discussed in the literature. Binary black holes may form via common envelope evolution (Belczynski et al. 2016), stable mass transfer (van den Heuvel et al. 2017; Neijssel et al. 2019; Bavera et al. 2020; Marchant et al. 2021), chemically homogeneous evolution (de Mink & Mandel 2016), and dynamical processes in dense stellar environments (Antonini & Rasio 2016). Early studies of massive LIGO black holes attributed the formation of these systems to pristine low-metallicity environments, which may be found in dwarf galaxies or massive galaxies at high redshift (Lamberts et al. 2016). Another possibility is that these massive black holes may form in the outer H I disks of spiral galaxies (Chakrabarti et al. 2017, 2018), where low metallicities are also prevalent (e.g., Kennicutt et al. 2003; Bresolin et al. 2012; Berg et al. 2020). Studies of the black hole-main sequence (BH-MS) binary population discovered from *Gaia* can now reveal potential differences with respect to the black hole-black hole (BH-BH) and black hole-neutron star (BH-NS) demographics. Although it is now clear that there is a strong observed anticorrelation between metallicity and close (periods $< 10^4$ d) binary fraction for solar type stars (Gao et al. 2014; Moe et al. 2019), the reverse trend is apparent for the high-mass X-ray binary population (Lehmer et al. 2021).

Searches for non-interacting black holes in binary systems with luminous companions have intensified in recent years, with a number of claimed detections (e.g., Liu et al. 2019; Rivinius et al. 2020; Jayasinghe et al. 2021, 2022; Lennon et al. 2021; Saracino et al. 2022). Most of these systems have been rapidly disputed or ruled out (e.g., Abdul-Masih et al. 2020; Bodensteiner et al. 2020; El-Badry & Quataert 2020; Eldridge et al. 2020; Shenar et al. 2020; El-Badry & Quataert 2021; El-Badry & Burdge 2022; El-Badry et al. 2022c,a; Frost

et al. 2022). To date only a few likely black holes¹ have survived this community vetting: a $> 3 M_{\odot}$ black hole with a red giant companion (Thompson et al. 2019, although see van den Heuvel & Tauris 2020a), a $> 9 M_{\odot}$ black hole orbiting a massive O star in the Large Magellanic Cloud (Shenar et al. 2022), and a $> 7 M_{\odot}$ black hole candidate orbiting the Galactic O star HD 130298 (Mahy et al. 2022). The object that we discuss in this paper has also been studied earlier by El-Badry et al. (2023a).

In work that is contemporaneous with ours (posted to the archive on September 14, 2022), El-Badry et al. (2023a) reported the independent discovery and analysis of the same source. Here we present our independent analysis of a main-sequence G star on an eccentric 185 d orbit around a $\sim 10 M_{\odot}$ dark companion, which we selected from the *Gaia* DR3 binary catalog. Given the now available data published from El-Badry et al. (2023a), we also present RV-only fits to the combined data set (ours and that of El-Badry et al.) as well as joint fits that incorporate both sets of RV data and the astrometry.

Our search for black hole candidates in binary systems with luminous companions begins with the *Gaia* DR3 catalog of binary masses. *Gaia* DR3 provides the largest sample of binary stars produced by the astronomical community thus far, yielding orbital solutions derived from astrometry and/or spectroscopy for $\sim 3 \times 10^5$ stars (Gaia Collaboration et al. 2022a; Halbwachs et al. 2022; Holl et al. 2022).

The paper is organized as follows. In §2, we briefly review our methodology, including our selection from the *Gaia* DR3 binary mass catalog, and additional tests. We provide all available photometry for the visible star, and describe our follow-up spectroscopic observations over the last several months and our procedures for measuring radial velocities. In §3, we describe our analysis of the observed spectral energy distribution (SED), fitting the photometric data with single source and multiple source models to find that the visible star is adequately described by a single stellar photosphere. In §4, we discuss the *Gaia* astrometric orbital solution, and compute orbits from our velocity data alone and from the combination of the velocities and the astrometry. We discuss our results in §5 and conclude in §6.

2. METHODS AND DATA COLLECTION

¹ Here we are setting aside several black hole binary candidates in globular clusters (Giesers et al. 2018, 2019), which may have different formation mechanisms.

The *Gaia* DR3 `non_single_stars` catalog contains 195,315 binary systems with lower limits on the mass of the secondary star. From this set, we selected those for which the secondary was constrained to be more massive than the primary and at least $5 M_{\odot}$, well above the mass range of white dwarfs and neutron stars. We removed double-lined spectroscopic binaries, and focused on bright ($G < 14$) companions that would allow for follow-up observations on a wide range of telescopes. For spectroscopic solutions, we retained sources that have at least ten RV points as reported by *Gaia* and significance > 5 . As an Astronomical Data Query Language search, this selection is given by

```
select * from
  gaiadr3.gaia_source inner join
  gaiadr3.nss_two_body_orbit
  using (source_id) inner join
  gaiadr3.binary_masses
  using (source_id)
where
  m2_lower > 5 and
  nss_solution_type != 'SB2' and
  phot_g_mean_mag < 14 and
  rv_nb_transits > 10 and
  significance > 5
```

In addition, we required that sources lie within ~ 0.5 magnitude of the *Gaia* main sequence. Sources with spectral energy distributions (SEDs) that are well-described by a single star and are located on the main sequence are strong candidates for hosting dark companions, as a luminous star that is more massive than the primary should be easily detectable (e.g., [El-Badry & Rix 2022](#)). Finally, we excluded sources that show variability in their TESS light curve that would indicate that they are eclipsing binaries. These cuts left us with a set of sources on which we obtained follow-up RV measurements (to be discussed elsewhere).

In the remainder of this paper, we describe our results and analysis of one star, *Gaia* DR3 4373465352415301632, for which an astrometric orbit was reported in DR3. We display the position of this object in the *Gaia* color-magnitude diagram in Figure 1. In the DR3 binary catalog, *Gaia* DR3 4373465352415301632 has a primary² mass of $0.95 M_{\odot}$, a secondary mass of $12.8_{-2.3}^{+2.8} M_{\odot}$, a period of 185.8 ± 0.3 d, and an eccentricity of 0.49 ± 0.07 . However, the only radial velocity information provided by *Gaia* is a single measurement of $v = 23.0 \pm 2.6$ km s⁻¹. No spectroscopic orbital solution is included in DR3, indicating that a spectroscopic orbit could not be determined from

the 13 independent radial velocity measurements obtained by *Gaia*. Because the astrometric orbit is at the extreme edge of the distribution of companion masses in the DR3 catalog, the lack of spectroscopic confirmation raises the concern that the astrometric solution, and the parameters derived from it, could be erroneous ([Halbwachs et al. 2022](#); [Gaia Collaboration et al. 2022a](#)). We focus in this paper on this source because it is the most compelling black hole candidate (meeting our criteria above) for which we have obtained RV data thus far. Spectroscopic observations for a limited number of other possible candidates are ongoing; analysis of those objects is beyond the scope of this paper.

We note that, in addition to the comprehensive analysis by [El-Badry et al. \(2023a\)](#), two other recent studies of the DR3 data set have also discussed this star as a candidate black hole binary. [Andrews et al. \(2022\)](#) selected 24 candidate compact object binaries from the DR3 astrometric orbital solutions, and obtained follow-up spectroscopy of some of them, including *Gaia* DR3 4373465352415301632. However, they discarded it because the orbital period is close to an integer multiple of the *Gaia* scanning law, suggesting that the derived orbit could be an artifact. [Shahaf et al. \(2022\)](#) used the astrometric mass ratio function to identify 177 candidate binaries containing compact objects. In their sample, *Gaia* DR3 4373465352415301632 has the highest secondary mass of the Class III sources, for which a compact object is the only viable type of companion, but no follow-up observations were obtained.

2.1. Photometry

We retrieved UV-IR photometry for this source from GALEX ([Martin et al. 2005](#)), SDSS ([Fukugita et al. 1996](#)), the APASS survey ([Henden et al. 2016](#)), *Gaia* DR3 ([Riello et al. 2021](#)), PanSTARRS ([Tonry et al. 2012](#)), SkyMapper ([Wolf et al. 2018](#)), 2MASS ([Skrutskie et al. 2006](#)), and WISE ([Wright et al. 2010](#)). Figure 2 displays the available photometry for this source and Table 1 lists the measurements and associated errors in each band. We analyze the spectral energy distribution of this source below and discuss our choice of photometry.

2.2. Spectroscopy

2.2.1. Observations and data reduction

We obtained follow-up high-resolution spectroscopy of *Gaia* DR3 4373465352415301632 in order to determine its stellar parameters, search for signatures of a second luminous component in the binary, and measure the radial velocity as a function of time. We observed the

² For this paper, we adopt the *Gaia* convention of referring to the luminous star as the primary and the non-luminous companion as the secondary even though the latter may be more massive.

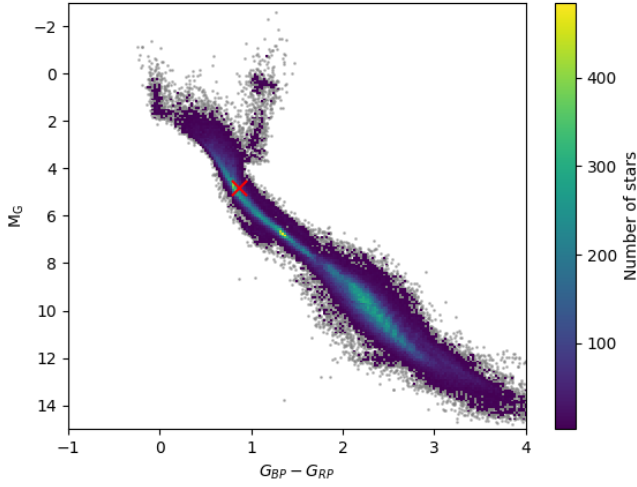


Figure 1. *Gaia* color-magnitude diagram. The extinction-corrected absolute magnitude and color of *Gaia* DR3 4373465352415301632, based on the *Gaia* parallax and G-band extinction, are marked with a red cross; the *Gaia* main-sequence is apparent.

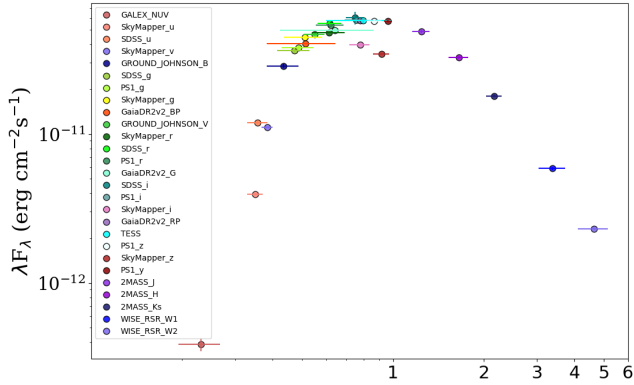


Figure 2. Available photometry of *Gaia* DR3 4373465352415301632 from the near-UV to the mid-infrared, with the data sources given in the legend.

star for five epochs with the Automated Planet Finder (APF) telescope (Vogt et al. 2014) at Lick Observatory, four epochs with the DEIMOS spectrograph (Faber et al. 2003) on the Keck II telescope, and obtained a high signal-to-noise ratio spectrum with the MIKE spectrograph (Bernstein et al. 2003) on the Magellan/Clay telescope (as well as a second, shorter MIKE spectrum) at Las Campanas Observatory.

The APF observations employed the Levy Spectrometer (Radovan et al. 2010) with a $2'' \times 8''$ slit, providing $R = 80000$ spectra covering 3730–10200 Å. We observed *Gaia* DR3 4373465352415301632 on 2022 June 28, 2022

Table 1. Photometry for *Gaia* DR3 4373465352415301632

Survey	Band	Magnitude	Magnitude Uncertainty
GALEX	NUV	20.281	0.115
SDSS	u	16.026	0.006
SDSS	g	14.504	0.003
SDSS	r	13.768	0.003
SDSS	i	13.462	0.004
SDSS	z	13.308	0.004
APASS	B	14.971	0.088
APASS	V	14.091	0.045
<i>Gaia</i> DR3	BP ^a	14.276	0.001
<i>Gaia</i> DR3	G ^a	13.772	0.001
<i>Gaia</i> DR3	RP ^a	13.101	0.001
Pan-STARRS	g	14.420	0.002
Pan-STARRS	r	13.781	0.002
Pan-STARRS	i	13.479	0.001
Pan-STARRS	z	13.346	0.002
Pan-STARRS	y	13.242	0.001
SkyMapper	u	16.041	0.010
SkyMapper	v	15.654	0.008
SkyMapper	g	14.252	0.005
SkyMapper	r	13.786	0.005
SkyMapper	i	13.450	0.004
SkyMapper	z	13.303	0.004
2MASS	J	12.244	0.024
2MASS	H	11.895	0.023
2MASS	Ks	11.780	0.023
WISE	W1	11.691	0.023
WISE	W2	11.717	0.022
WISE	W3	11.671	0.232

^aThe formal uncertainties on the *Gaia* DR3 photometry are smaller than listed here, but are rounded to 1 mmag for convenience and because calibration errors between surveys will limit cross-survey comparisons to a coarser level.

August 28, 2022 September 2, 2022 September 12, and 2022 October 4, obtaining three 1000 s exposures per epoch. The APF spectra were reduced with the California Planet Search pipeline (Butler et al. 1996; Howard et al. 2010; Fulton et al. 2015).

We observed *Gaia* DR3 4373465352415301632 with Magellan/MIKE for 2700 s on 2022 August 22, using a $0''.7$ slit to obtain an $R \approx 30000$ spectrum from 3300–9400 Å. We reduced the MIKE spectrum with the

Carnegie Python data reduction package (Kelson 2003). To provide a comparison spectrum, we also obtained MIKE observations of the G1.5V radial velocity standard star HD 126053. Portions of the spectra of these two stars are displayed in Fig. 3. We also observed *Gaia* DR3 4373465352415301632 for 745 s with MIKE during twilight on 2022 October 13 to obtain an additional velocity measurement. Fig. 4 compares the two MIKE spectra of *Gaia* DR3 4373465352415301632, which represent the radial velocity extremes in our data set.

We observed *Gaia* DR3 4373465352415301632 with DEIMOS on 2022 September 19, 2022 September 24, 2022 September 27, and 2022 October 28 using the 1200G grating and a $0''.7$ long slit to obtain $R \approx 7000$ spectra from 6500–9000 Å. A single 300 s exposure was obtained in twilight on each night. We reduced the data with a modified version of the DEEP2 reduction pipeline (Cooper et al. 2012; Newman et al. 2013; Kirby et al. 2015). The long-slit mask employed for these observations did not contain enough slits to adequately constrain the quadratic correction to the sky line wavelengths as a function of position on the mask described by Kirby et al. (2015). Instead, we examined the night sky emission line wavelengths in the extracted spectrum, and used the measured wavelength shifts near the A-band and Ca triplet lines (which ranged from 0–4 km s⁻¹) to correct the wavelength scale.

2.2.2. Velocity measurements

We measured the velocity of *Gaia* DR3 4373465352415301632 from the APF and MIKE spectra by performing χ^2 fits to high S/N spectra of radial velocity standard stars shifted to the rest frame. The velocity template for the MIKE spectra was HD 126053, for which we assumed a velocity of $v_{hel} = -19.21$ km s⁻¹ from *Gaia* DR3, which is in excellent agreement with the measurement of $v_{hel} = -19.45$ km s⁻¹ from Stefanik et al. (1999). For the APF velocity measurements, we used an APF observation of the G2V standard star HD 12846 (Gray et al. 2003; Soubiran et al. 2018). We assumed the *Gaia* DR3 velocity of $v_{hel} = -4.65$ km s⁻¹, which is within 0.2 km s⁻¹ of the pre-*Gaia* measurement of Soubiran et al.. The fit procedures were based on those described by Simon et al. (2017) and subsequent papers, adapted for echelle spectroscopy. We fit each order of the target spectra independently with the matching order of the template spectrum, discarding orders or portions of orders affected by telluric or interstellar absorption. For the MIKE observation we used only the data from the red spectrograph (covering ~ 4900 – 8900 Å) for velocities because the stellar con-

tinuum was more difficult to define at blue wavelengths and the 23 clean red orders already provided plenty of signal. The S/N of the APF data was much lower, but the velocity could still be determined accurately over ~ 30 spectral orders from ~ 4500 – 6800 Å. For each observation, we averaged the velocities from all measured orders. The resulting statistical uncertainty was ~ 0.1 km s⁻¹ for both the MIKE spectrum and the APF spectra. However, we imposed a systematic error floor of 1.0 km s⁻¹ for MIKE based on the results of Ji et al. (2020). Given the potential for velocity offsets between different instruments, we assumed the same minimum uncertainty of 1.0 km s⁻¹ for the APF observations.

For the DEIMOS spectrum, we used the set of radial velocity templates described by Kirby et al. (2015), fitting only to the Ca triplet wavelength range. We found that the metal-poor K1 dwarf HD 103095 produced the best match to the *Gaia* DR3 4373465352415301632 spectrum, so we used that template to determine the velocity. The velocity of the HD 103095 template spectrum was tied to that of the metal-poor giant HD 122563, for which we assumed a velocity of -26.51 km s⁻¹ (Chubak et al. 2012), which agrees with the *Gaia* measurements within 0.4 km s⁻¹. We corrected for slit centering errors by carrying out a separate fit to the telluric A-band absorption of the rapidly rotating star HR 7346 (Sohn et al. 2007; Simon & Geha 2007). Based on the scatter of sky lines around their true wavelengths, we assume a velocity uncertainty of 2.0 km s⁻¹ for each DEIMOS measurement (cf. Simon & Geha 2007; Kirby et al. 2015).

All of our velocity measurements, along with the two archival data points from LAMOST DR7 (Cui et al. 2012; Luo et al. 2022), are listed in Table 2.

3. RESULTS & ANALYSIS

3.1. The Spectral Energy Distribution

All of the archival photometry of *Gaia* DR3 4373465352415301632 that we were able to locate, including measurements from GALEX (Morrissey et al. 2007), SDSS DR16 Ahumada et al. (2020), APASS DR10 (Henden 2019), Pan-STARRS DR2 (Flewelling et al. 2020), SkyMapper DR2 (Onken et al. 2019), 2MASS (Cutri et al. 2003), and WISE (Cutri et al. 2021), is displayed in Figure 2 and listed in Table 1. As is clear, the SkyMapper v, i, z bands are discrepant with other photometric measurements at comparable wavelengths, and we therefore exclude them from our SED fits. Using the publicly available SED fitting code ARIADNE (Vines & Jenkins 2022), we fit the observed photometry (excluding SkyMapper as well as the wide *Gaia* bands) to derive stellar parameters. Although *Gaia* of-

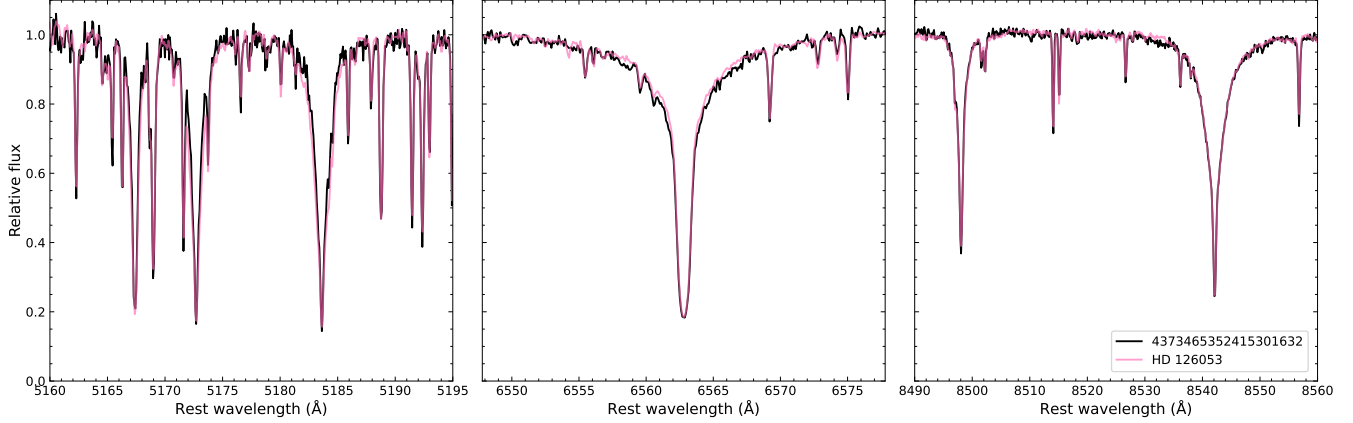


Figure 3. Selected portions of the Magellan/MIKE spectrum of *Gaia* DR3 4373465352415301632 (from left to right: the Mg triplet lines, $H\alpha$, and the Ca triplet). The spectrum of HD 126053, which has a spectral type of G1.5V (Gray et al. 2003), is overplotted in pink as a comparison. The close resemblance between the two stars in terms of line strengths and profiles is evident. The stellar parameters of HD 126053 are $T_{\text{eff}} = 5700$ K, $\log g = 4.5$, $[\text{Fe}/\text{H}] = -0.35$ (e.g., Brewer et al. 2016; Casali et al. 2020). The small deviations in the wings of some strong lines are likely caused by a combination of continuum normalization uncertainties, and the ~ 200 K difference in temperature between the two stars.

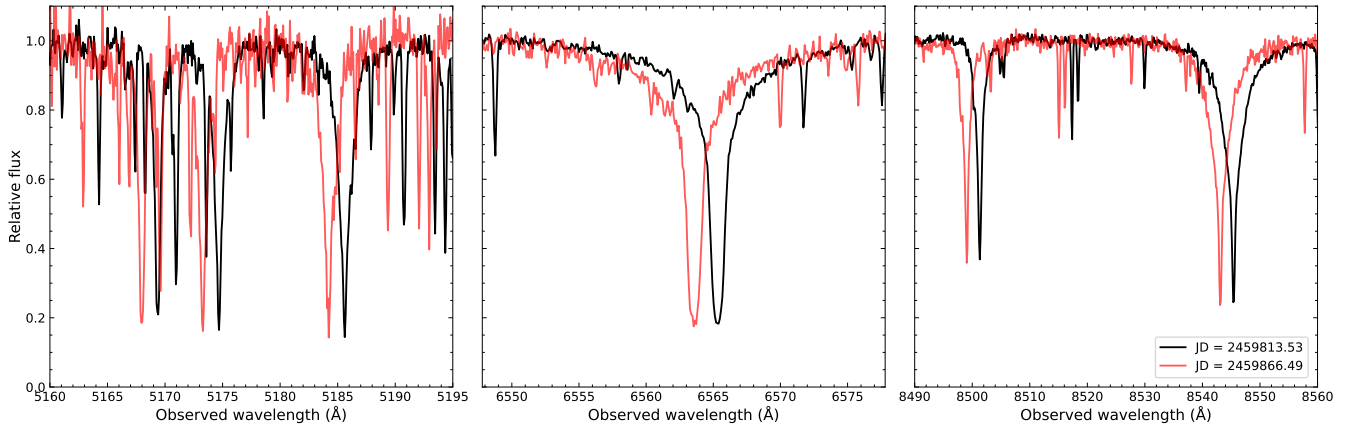


Figure 4. Selected portions of the Magellan/MIKE spectrum of *Gaia* DR3 4373465352415301632 (the Mg triplet lines, $H\alpha$, and the Ca triplet), shown here in the observed frame at the radial velocity extremes spanned by our data set.

fers extremely precise optical photometry of *Gaia* DR3 4373465352415301632, we note that there may be contamination in the G_{BP} and G_{RP} bands as a result of the star’s location in the direction of the Galactic bulge. The $\text{phot_bp_rp_excess_factor}$ for this source is 1.24 and the $G_{BP} - G_{RP}$ color is 1.17, which indicates that the blending probability is $\sim 30\%$ (Riello et al. 2021).

The resultant posterior distributions are shown in the corner plot for the stellar parameters, along with the best-fit extinction in Figure 5. ARIADNE fits broadband photometry to a variety of stellar atmosphere models. In this case, the best fit is obtained with the Phoenix models (Husser et al. 2013). Here, we have used a prior on the distance that is consistent with the measured *Gaia* parallax for this source. Including the *Gaia* G -

band magnitude in the fit does not significantly change any of the derived parameters. We obtain similar values for the effective temperature and other derived parameters fitting only to GALEX photometry, along with B and V bands from APASS, SDSS g, r, i, z , 2MASS J, H, K_s , and WISE photometry. Similar posterior distributions are also obtained if Pan-STARRS photometry is used instead of SDSS. The best-fit ARIADNE parameters are: $T_{\text{eff}} = 5796^{+93}_{-153}$ K, $\log g = 4.26^{+0.24}_{-0.27}$, $R = 1.02^{+0.031}_{-0.029} R_{\odot}$, and $[\text{Fe}/\text{H}] = -0.24^{+0.09}_{-0.08}$. As the corner plot shows, the posterior distributions are tightly constrained. The SED fit, along with the residuals, is shown in the bottom panel of Figure 5.

We have also used the BaSeL model spectral library (Lejeune et al. 1997, 1998) to fit the observed photome-

Table 2. Radial Velocity Measurements for Gaia DR3 4373465352415301632

Julian Date	Heliocentric Velocity [km s ⁻¹]	Velocity Uncertainty [km s ⁻¹]	Telescope/Instrument
2457881.29	20.0	4.1	LAMOST
2458574.36	8.9	5.6	LAMOST
2459758.93	50.5	1.0	APF
2459813.53	90.3	1.0	Magellan/MIKE
2459819.68	67.6	1.0	APF
2459825.76	49.4	1.0	APF
2459835.65	31.0	1.0	APF
2459842.72	22.6	2.0	Keck/DEIMOS
2459847.71	17.6	2.0	Keck/DEIMOS
2459850.71	15.4	2.0	Keck/DEIMOS
2459857.65	13.1	1.0	APF
2459866.49	11.1	1.0	Magellan/MIKE
2459881.69	11.8	2.0	Keck/DEIMOS

try with both a combined χ^2 and genetic algorithm optimization and a Markov Chain Monte Carlo (MCMC) approach. Here we assume a [Fitzpatrick \(1999\)](#) extinction law with $R_V = 3.1$ and reddening $E(B - V) = 0.3$ mag. The best-fit SEDs are shown in Figure 6a for a single source, and the fit assuming two sources is shown in Figure 6b. In the single source case, we obtain a reduced χ^2 of 3.7, best-fit parameters $T_{\text{eff}} = 5927$ K, $\log g = 4.0$, $L = 1.08 L_{\odot}$ and metallicity of $Z = 0.009$. For a two source fit, we obtain a reduced χ^2 of 5.5, with $T_{\text{eff}} = 6241$ K, $\log g = 4.99$, $L = 0.42 L_{\odot}$, and $Z = 0.0006$ for the hotter component and $T_{\text{eff}} = 5763$ K, $\log g = 4.01$, $L = 0.67 L_{\odot}$, and $Z = 0.01$ for the cooler component. Although the raw χ^2 value does improve upon adding a second component (17 for the composite spectrum vs. 25 for the single SED fit), this is not enough to compensate for the increase in the number of model parameters in the reduced χ^2 . We conclude that there is no significant evidence in the SED for the presence of more than one luminous component.

3.2. Spectroscopic Analysis and Stellar Parameter Estimation

3.2.1. Full spectral fitting

Visual examination of the MIKE spectrum of Gaia DR3 4373465352415301632 shows that it closely resembles an early G star (see Fig. 3). No sign of a secondary component is visible in either the metallic or

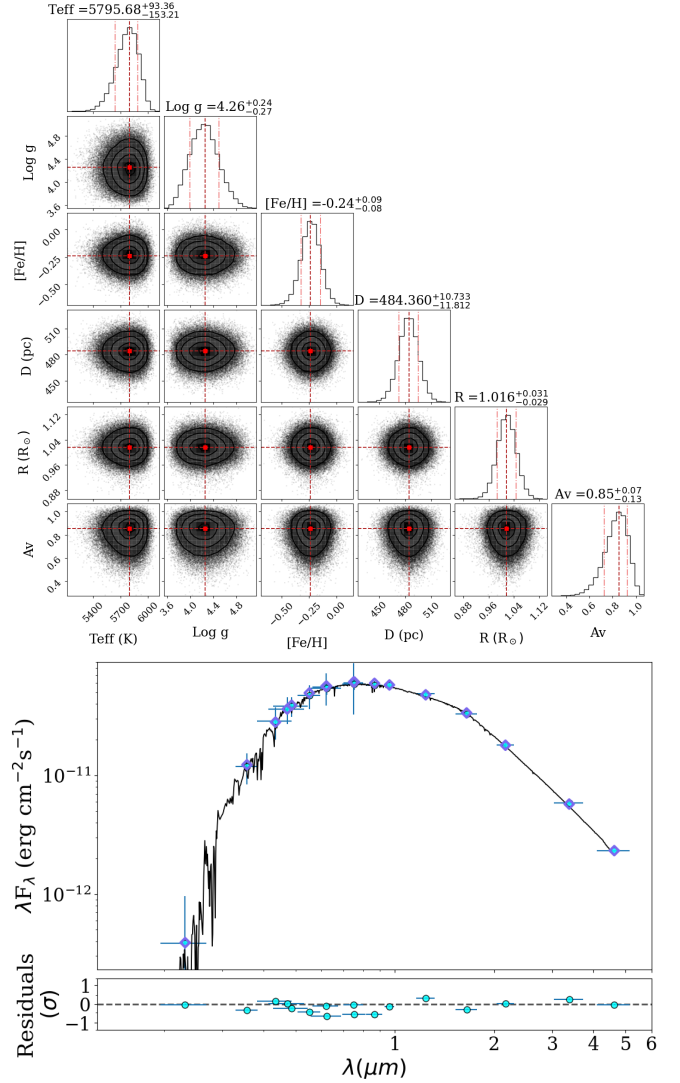


Figure 5. (top) Posterior distributions of stellar parameters from ARIADNE using all available photometry except SkyMapper and *Gaia*, with the distance prior set from the measured *Gaia* parallax. (bottom) Resultant best-fit SED. There is no evidence for an excess at short or long wavelengths that could indicate a second source contributing to the observed fluxes. The same points are shown in the residual plot below in circles (in the SED plot, they are overplotted with diamonds).

hydrogen lines. Given the spectral resolution, a companion star that makes a non-negligible contribution to the flux should be detectable unless its velocity is within ~ 10 km s⁻¹ of that of the primary. As we will show below, the velocity of the primary at the time of observation was more than 40 km s⁻¹ away from the center-of-mass velocity of the system (also see Fig. 4), which indicates that the secondary spectrum should be resolv-

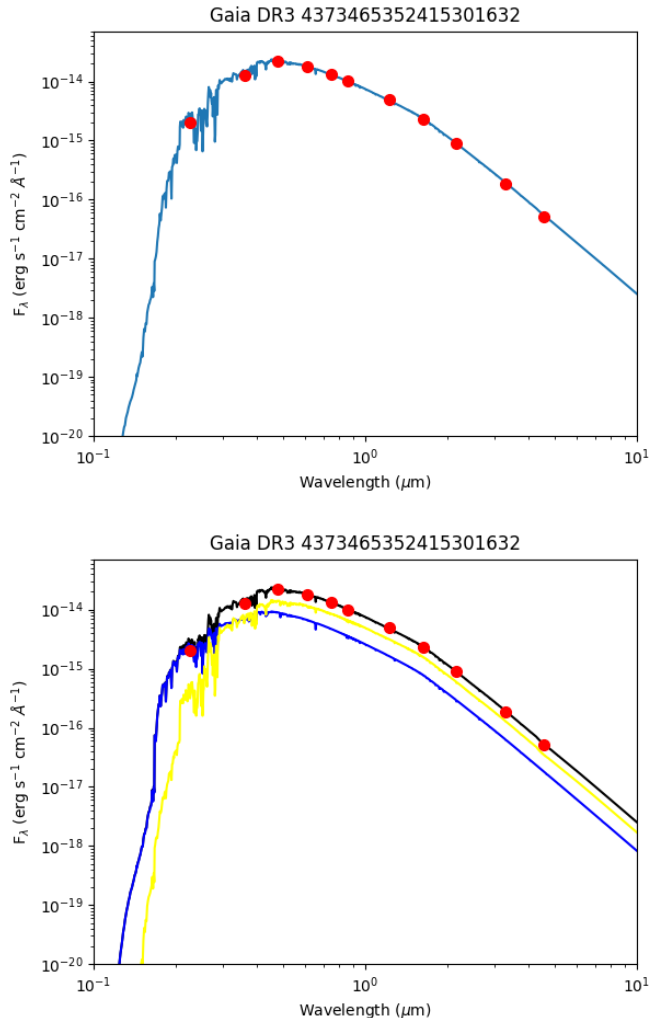


Figure 6. (a) Single SED fit using the BaSeL model and the Fitzpatrick (1999) extinction law. (b) Composite SED fit, with the cooler component shown in yellow, hotter component shown in blue, and the composite spectrum shown in black.

able from the primary at this epoch if it is a luminous main-sequence star.

To provide an initial estimate of the stellar parameters from its spectrum rather than the broadband photometry, we fit the MIKE spectrum with the empirical spectral fitting code *SpecMatch-Emp* (Yee et al. 2017). Using the spectral range 5100–5700 Å, the best-fit parameters determined from a linear combination of stars in the template library are: $T_{\text{eff}} = 5917 \pm 110$ K, $R = 1.20 \pm 0.18 R_{\odot}$, $\log g = 4.24 \pm 0.14$,³ and $[\text{Fe}/\text{H}] =$

³ To determine $\log g$, we make use of the result from the detailed spectroscopic analysis below that the mass of the star is $0.91 M_{\odot}$.

-0.22 ± 0.09 , with HD 44985 as the single closest match to *Gaia* DR3 4373465352415301632. These parameters are in excellent agreement with those from the SED fit.

3.2.2. Fundamental and photospheric stellar parameters

Next, we determined the stellar parameters of *Gaia* DR3 4373465352415301632 more rigorously using a combination of the classical spectroscopic approach⁴ and a comparison with theoretical isochrones to infer accurate, precise, and self-consistent parameters.

The inputs to this parameter inference procedure include the equivalent widths of Fe I and Fe II atomic absorption lines, as well as multiwavelength photometry from *Gaia* DR3 G-band (Riello et al. 2021) and 2MASS (J, H, and K_s), the *Gaia* DR3 parallax (Lindgren et al. 2021a), and we adopt the V-band extinction from the three-dimensional Stilism reddening map (Lallement et al. 2014; Capitano et al. 2017; Lallement et al. 2018). The absorption line data are based on the line lists presented in Meléndez et al. (2014) and Reggiani & Meléndez (2018). We measured the equivalent widths by fitting Gaussian profiles with the Spectroscopy Made Harder (*smhr*) software package to the continuum-normalized MIKE spectrum. The continuum normalization was performed using *smhr*. We assume solar abundances from Asplund et al. (2021) and follow the steps described in Reggiani et al. (2022b,a) to obtain the fundamental and photospheric stellar parameters from a combination of spectral information and a fit to the MESA Isochrones and Stellar Tracks (MIST; Dotter 2016; Choi et al. 2016; Paxton et al. 2011, 2019) stellar models. We do the fitting with the *isochrones* package⁵ (Morton 2015), which uses *MultiNest*⁶ (Feroz & Hobson 2008; Feroz et al. 2009, 2019) via *PyMultiNest* (Buchner et al. 2014).

Our derived fundamental and photospheric parameters for *Gaia* DR3 4373465352415301632 are listed in Table 3. Its position relative to the MIST isochrones is illustrated in Figure 7. The effective temperature is in excellent agreement with the values determined from the single-source SED fit as well as the full spectral fitting. According to the effective temperature calibration given by Gray & Corbally (2009), the spectral classification would be G0. The surface gravity required to enforce ionization balance on the Fe lines is somewhat

⁴ Based on simultaneously minimizing the difference between the abundances determined from Fe I and Fe II lines, as well as their dependencies on transition excitation potential and reduced equivalent width.

⁵ <https://github.com/timothydmorton/isochrones>

⁶ <https://ccpforge.cse.rl.ac.uk/gf/project/multinest/>

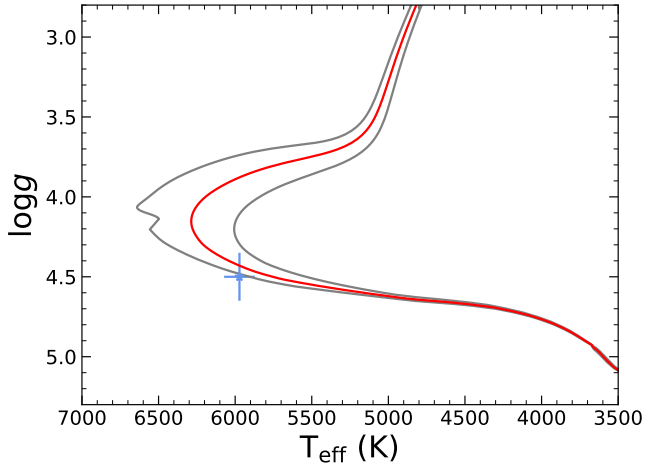


Figure 7. Effective temperature and surface gravity of *Gaia* DR3 4373465352415301632 compared to MIST isochrones. The blue point shows the derived position of the star and the red curve is the $0.91 M_{\odot}$ isochrone that provides the best fit to the combined photometric and spectroscopic data. The gray curves represent $0.89 M_{\odot}$ and $0.93 M_{\odot}$ isochrones for comparison.

Table 3. Derived Stellar Parameters

Property	Value	Unit
Effective temperature (T_{eff})	5972 ± 100	K
Surface gravity ($\log g$)	4.54 ± 0.15	$\log \text{cm s}^{-2}$
Metallicity ($[\text{Fe}/\text{H}]$)	-0.30 ± 0.10	
Microturbulent velocity (ξ)	1.10 ± 0.10	km s^{-1}
Stellar mass (M_{*})	0.91 ± 0.10	M_{\odot}
Stellar radius (R_{*})	1.003 ± 0.075	R_{\odot}
Luminosity (L_{*})	1.186 ± 0.232	L_{\odot}
Isochrone-based age (τ_{iso})	7.1 ± 3.8	Gyr

NOTE—The parameters listed here are determined via the combined analysis of the high-resolution stellar spectrum along with theoretical isochrones, as described in Section 3.2.2.

higher than determined via other techniques, but the disagreement is only at the 1.6σ level. The spectroscopic metallicity of *Gaia* DR3 4373465352415301632 is also modestly lower than the photometric value. The overall good agreement on the stellar parameters achieved through multiple independent methods indicates that systematic uncertainties, e.g., related to the choice of stellar evolution tracks, are smaller than the adopted uncertainties (Table 3). We conclude that *Gaia* DR3 4373465352415301632 is an old, moderately metal-poor main sequence star, slightly less massive than the Sun.

3.2.3. Chemical abundances

We used the photospheric stellar parameters from Table 3 to calculate the abundances of C I, O I, Na I, Mg I, Al I, Si I, S I, K I, Ca I, Sc II, Ti I, Ti II, V I, Cr I, Cr II, Mn I, Fe I, Fe II, Co I, Ni I, Cu I, Zn I, Sr II, Y II, Zr II, Ba II, and Ce II, from the equivalent widths (EWs) of spectroscopic absorption lines. We measured equivalent widths from the continuum-normalized MIKE spectrum by fitting Gaussian profiles with *smhr*. We use the 1D plane-parallel, α -enhanced, ATLAS9 model atmospheres (Castelli & Kurucz 2003) and the 2019 version of MOOG (Snedden 1973) to infer elemental abundances based on each equivalent width measurement, initially assuming local thermodynamic equilibrium (LTE). Our calculations include hyperfine structure splitting for Sc II (based on the Kurucz line list⁷), V I (Prochaska et al. 2000), Mn I (Prochaska & McWilliam 2000; Blackwell-Whitehead et al. 2005), Cu I (Prochaska et al. 2000, and Kurucz line lists), and Y II (Kurucz linelists), and we account for isotopic splitting for Ba II (McWilliam 1998). We report the adopted atomic data, equivalent width measurements, and individual line-based abundances in Table 4. Our final abundances are reported in Table 5.

When possible, we update our elemental abundances derived under the assumptions of LTE to account for departures from LTE (i.e., non-LTE corrections) by interpolating published grids of non-LTE corrections for several elements. We make use of 3D non-LTE corrections for carbon and oxygen (Amarsi et al. 2019), and 1D non-LTE corrections for sodium (Lind et al. 2011), aluminum (Amarsi et al. 2020), silicon (Amarsi & Asplund 2017), potassium (Reggiani et al. 2019), calcium (Amarsi et al. 2020), iron (Amarsi et al. 2016), and barium (Amarsi et al. 2020). The NLTE-corrected abundances are listed in Table 5.

The abundance analysis shows that *Gaia* DR3 4373465352415301632 is a mildly α -enhanced star ($[\alpha/\text{Fe}] \sim 0.1$), as expected for its metallicity. The iron-peak and neutron-capture elemental abundances are also fully compatible with the typical values for this metallicity range, based on galactic chemical evolution models (e.g., Kobayashi et al. 2020) and large spectroscopic surveys (e.g., Amarsi et al. 2020). We do not see any sign of the large enhancements in light elements and α elements that have been detected in some X-ray binary compan-

⁷ <http://kurucz.harvard.edu/linelists.html>

Table 4. Atomic data, Equivalent Widths and line Abundances. Full version online.

Wavelength (Å)	Species	Excitation Potential (eV)	$\log(gf)$	EW (mÅ)	$\log_\epsilon(X)$
6154.225	Na I	2.102	-1.547	20.80	5.993
6160.747	Na I	2.104	-1.246	31.52	5.927
4571.095	Mg I	0.000	-5.623	89.51	7.395
4730.040	Mg I	4.340	-2.389	43.79	7.381
5711.088	Mg I	4.345	-1.729	80.01	7.244
6318.717	Mg I	5.108	-1.945	26.75	7.284
5260.387	Ca I	2.521	-1.719	23.01	6.139
5512.980	Ca I	2.933	-0.464	63.20	5.966

NOTE—This table will be published in its entirety as a machine-readable table. A portion is shown here for guidance regarding its form and content.

ions (e.g., Orosz et al. 2001; González Hernández et al. 2008; Suárez-Andrés et al. 2015; Casares et al. 2017).

4. ORBIT FITTING

Based on the *Gaia* astrometry and our radial velocity measurements, the binary orbit of *Gaia* DR3 4373465352415301632 can be determined astrometrically, spectroscopically, or using a combination of both types of data. In order to test the consistency of the velocities with the *Gaia* astrometric orbit, we consider each of these cases in turn. We fit Keplerian orbits to the RV data using the adaptation of the `orvara` code (Brandt et al. 2021) presented in Lipartito et al. (2021).

In this section, we briefly discuss the *Gaia* orbital constraints and then present our orbital fits using only RVs. For joint astrometric+spectroscopic fits, we cannot use `orvara` directly with *Gaia* astrometry because the individual astrometric measurements are not given in DR3. We have only a set of best-fit parameters and a covariance matrix. As a result, we incorporate constraints from *Gaia* by conditioning our RV fits on the *Gaia* results. (An alternate approximate approach would be to determine the times that targets cross the *Gaia* focal plane and use that as an estimate of the times of observation.) We discuss this approach and our results in Section 4.3.

4.1. Astrometry Only

The *Gaia* DR3 `non_single_stars` catalog provides orbital parameters for *Gaia* DR3 4373465352415301632 based on a fit to the individual astrometric measurements obtained by *Gaia*. However, the astrometric measurements themselves will not be available until the fourth *Gaia* data release ~ 3 years from the time of this

writing. The parameters listed directly in the catalog include the period P , the time of periastron T_0 , the eccentricity e , the secondary mass M_2 , and the Thiele-Innes (TI) elements A , B , F , and G . Following the method of Binnendijk (1960), as presented by Halbwachs et al. (2022), we use the TI elements to compute the semi-major axis a , the position angle of the ascending node Ω , the longitude of periastron ω , and the inclination i . The values of these parameters are listed in Table 6. We note that these calculations are based on the results reported in the two body orbit catalog and the binary mass catalog from *Gaia* Collaboration et al. (2022a).

The TI elements, together with the eccentricity, describe an orbit in the plane of the sky. We generate 50 random realizations of measurements drawn from the *Gaia* best-fit values and covariance matrix. We then plot the sky paths given by the eccentricities and TI elements. Figure 8 shows these sky paths about the barycenter; the best-fit orbit reported by *Gaia* DR3 is shown as a thicker black line. The orbit has a semimajor axis of 2.98 ± 0.22 mas, with the major axis oriented nearly east-west.⁸

4.2. Radial Velocity Data Only

We fit the radial velocity data using the adaptation of `orvara` (Brandt et al. 2021) described in Lipartito et al. (2021). This remains an MCMC-based fitting approach,

⁸ We note that the perpendicular orientation shown by El-Badry et al. (2023a) is a result of an inconsistency in a plotting routine (K. El-Badry 2023, private communication).

Table 5. Chemical Abundances

Species	N	$\log(\epsilon_X)$	[X/Fe]	$\sigma_{[X/Fe]}$
C I	4	8.01	-0.15	0.09
O I	3	8.65	0.26	0.03
Na I	2	5.96	0.04	0.03
Mg I	4	7.33	0.08	0.04
Al I	5	6.08	-0.05	0.02
Si I	11	7.27	0.06	0.03
S I	4	6.85	0.03	0.01
K I	1	5.18	0.42	0.01
Ca I	10	6.06	0.06	0.02
Sc II	4	2.94	0.10	0.09
Ti I	9	4.60	-0.07	0.03
Ti II	10	4.80	0.13	0.04
V I	3	3.51	-0.09	0.02
Cr I	8	5.26	-0.06	0.02
Cr II	5	5.24	-0.07	0.03
Mn I	6	4.88	-0.23	0.05
Fe I	79	7.16
Fe II	18	7.15
Ni I	14	5.94	0.04	0.03
Cu I	2	3.79	-0.09	0.02
Zn I	2	4.25	-0.01	0.07
Sr I	1	2.41	-0.12	0.00
Y II	3	1.82	-0.08	0.05
Zr II	1	2.29	-0.00	0.03
Ba II	3	2.12	0.15	0.05
Ce II	1	1.55	0.27	0.03
non-LTE Corrected Abundances				
C I	4	8.07	-0.04	0.16
O I	3	8.57	0.24	0.03
Na I	2	5.85	-0.01	0.04
Al I	2	6.07	0.00	0.01
Si I	11	7.25	0.10	0.08
K I	1	4.74	0.03	...
Fe I	79	7.18
Fe II	18	7.22
Ba II	3	1.96	0.06	0.03

but differs from the main version of `orvara` in several ways:

- it fits only for the RV parameters of period, eccentricity, RV semiamplitude, periastron time, argument of periastron, and RV zero point;
- the argument of periastron refers to the star (as is the definition for *Gaia* astrometry);

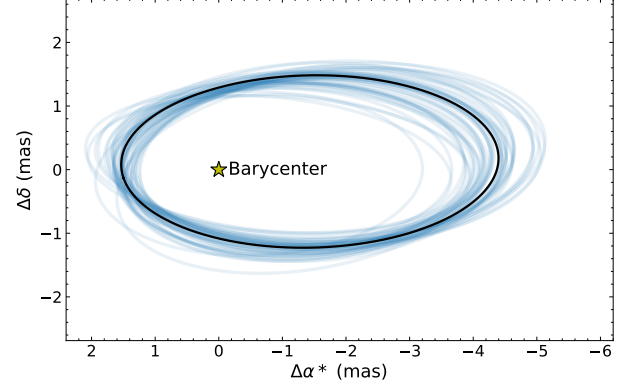


Figure 8. Astrometric orbit determined from the *Gaia* DR3 astrometric orbital solution as described in the text. The best-fit orbit calculated directly from the *Gaia* parameters is plotted as the thick black curve, and the thin blue curves represent orbits drawn randomly from the posterior distribution.

- only the RV zero point (barycenter RV of the system) is analytically marginalized off.

We use uniform priors on all of the RV parameters: period, semiamplitude, eccentricity, periastron time, RV zero point, and (stellar) argument of periastron. We find a highly multimodal posterior, with orbital solutions at periods of ~ 142 d, ~ 164 d, ~ 184 d, ~ 220 d, and additional possible periods out to at least 1000 days. The top panel of Figure 9 shows the wide range of RV orbits consistent with our *Gaia* DR3 4373465352415301632 velocities. The fits to the data are satisfactory, with a best-fit χ^2 of 3 for 13 data points with six free parameters, i.e., seven degrees of freedom.

Because one of our main goals is to determine whether the *Gaia* astrometric orbital solution is correct, we restrict the subsequent analysis of our RV data to solutions with a period range within ± 10 days of the *Gaia* orbital period of ~ 185 d, discarding those with shorter or longer periods. A similar procedure was adopted by [El-Badry et al. \(2023a\)](#) in their analysis since their RV data (although more extensive than ours) also yields multiple period solutions. However, as we note below, the combination of our RV data and that of [El-Badry et al. \(2023a\)](#) gives a unimodal solution for the period, which is not possible using either data set alone. This result is illustrated in Figure 9b, where the combined RV data uniquely determine the orbital period without reference to the *Gaia* astrometric solution. The fit to the combined RV data set remains formally good, with a best-fit χ^2 of 24 for 52 total radial velocity measurements and six free parameters (46 degrees of freedom). The low χ^2 value suggests that, if anything, the RV errors and, by

Table 6. Orbital Solutions for *Gaia* DR3 4373465352415301632 for the dataset listed in Table 2

Parameter	Value
Astrometric fit	
P	185.77 ± 0.31 d
T_0	2457377.0 ± 6.3 d
e	0.49 ± 0.07
a	2.98 ± 0.22 mas
i	$121^\circ.3 \pm 3.5$
Ω	$89^\circ.6 \pm 3.8$
ω	$-10^\circ.6 \pm 11.9$
M_2	$12.8^{+2.8}_{-2.3} M_\odot$
RV fit	
P	$184.28^{+0.75}_{-0.89}$ d
T_0	2459802.4 ± 3.0 d
e	$0.411^{+0.034}_{-0.021}$
ω	$19^\circ.1^{+6.0}_{-6.6}$
K_1	$60.6^{+10.0}_{-5.8}$ km s $^{-1}$
γ	$47.8^{+2.2}_{-1.4}$ km s $^{-1}$
f	$3.2^{+1.6}_{-0.9} M_\odot$
Joint fit	
P	$185.41^{+0.101}_{-0.087}$ d
T_0	$2459757.9^{+1.2}_{-1.5}$ d
e	$0.456 \pm .023$
a	$1.357^{+0.069}_{-0.061}$ AU
i	123.6 ± 1.6
Ω	$96^\circ.2^{+2.3}_{-2.0}$
ω	$10^\circ.4^{+2.7}_{-2.0}$
M_2	$11.33^{+1.57}_{-1.32} M_\odot$

extension, our derived parameter uncertainties, may be overestimated.

The spectroscopic orbital parameters from the MCMC fit to our RV data set (the velocities listed in Table 2), restricted to periods between 175 and 195 days, are listed in the second section of Table 6. Figure 10 shows the corner plot of the posterior distribution. Using all available RVs gives the posterior distributions shown in Figure 11 and the best-fit parameters listed in the top section of Table 7, whereby the combination of both data sets yields very precise constraints on all parameters that can be determined with RV data. The radial velocity curve and the phase-folded radial velocity curve with residuals are displayed in Figure 12 for both our RV data alone and all available RV data. Although our RV data allow a wide range of possible orbits, especially at phases near 0 and 1, the inclusion of data from [El-Badry et al. \(2023a\)](#) restricts the range of possible orbits sig-

Table 7. Orbital Solutions for *Gaia* DR3 4373465352415301632 using all available data

Parameter	Value
RV fit	
P	$184.52^{+0.66}_{-0.80}$ d
T_0	2459801.16 ± 0.12 d
e	$0.4368^{+0.0036}_{-0.0037}$
ω	$16^\circ.10 \pm 0.63$
K_1	$65.58^{+0.31}_{-0.30}$ km s $^{-1}$
γ	$48.48^{+0.36}_{-0.36}$ km s $^{-1}$
f	$3.92^{+0.042}_{-0.042} M_\odot$
Joint fit	
P	$185.52^{+0.08}_{-0.08}$ d
T_0	2459759.3 ± 1.1 d
e	$0.439^{+0.003}_{-0.003}$
a	$1.258^{+0.011}_{-0.010}$ AU
i	$126^\circ.80^{+0.62}_{-0.63}$
Ω	$98^\circ.71^{+1.97}_{-2.01}$
ω	$15^\circ.89 \pm 0.61$
M_2	$9.326^{+0.216}_{-0.208} M_\odot$

nificantly. Just 0.4% of the points in the chain lie away from the mode at $P \approx 185$ d, in a much sparser cluster at $P \approx 218$ d. We obtain very similar results using different orbit-fitting packages such as [TheJoker \(Price-Whelan et al. 2017\)](#) or [exoplanet \(Foreman-Mackey et al. 2021a,b\)](#).

The mass function derived from our period-restricted spectroscopic orbital solution is $f = 3.2^{+1.6}_{-0.9} M_\odot$. Combined with the primary mass determined from the spectral analysis, the corresponding minimum secondary mass is $4.6 M_\odot$, consistent with the companion being a black hole. However, because our spectroscopic measurements missed the maximum radial velocity at the periastron of the orbit, our constraint on the velocity semi-amplitude K_1 is not very strong, as is apparent from the definition of the mass function:

$$f = \frac{PK_1^3}{2\pi G} (1 - e^2)^{3/2} = \frac{M_2^3 \sin^3 i}{(M_1 + M_2)^2}, \quad (1)$$

where P is the orbital period, and M_1 and M_2 are the masses of the two stars. The cubic dependence of the mass function on K_1 then results in a large uncertainty in the mass function and the mass of the secondary, such that with our radial velocities alone we cannot completely exclude masses below $4 M_\odot$. The derived constraints on the spectroscopic mass function improve significantly when using all available RV data, combin-

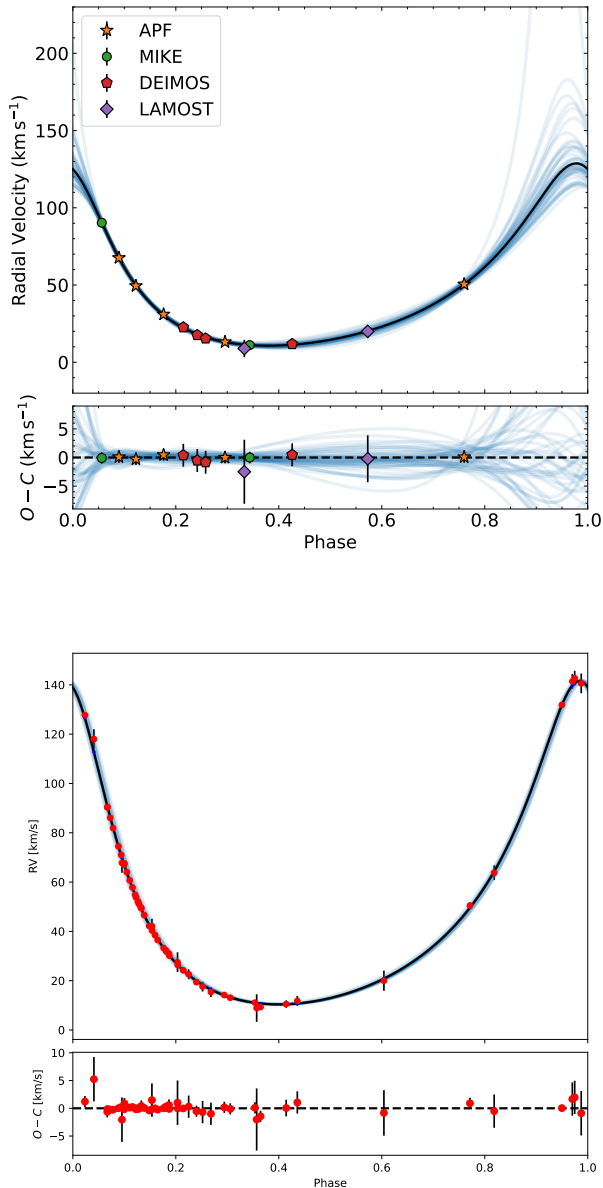


Figure 9. (Top) Radial velocity solution for *Gaia* DR3 4373465352415301632, for the velocity measurements listed in Table 2. The black curve is the most likely MCMC orbital solution determined from the spectroscopic measurements alone, and the light blue curves are a random set of MCMC samples. Many periods are consistent with the RV data. (Bottom) Radial velocity solution including data from Table 2 and from El-Badry et al. (2023a). This fit yields a unimodal solution for the period even without incorporating any information from the astrometric solution (0.4% of the points in the chain are at $P \approx 218$ d).

ing our measurements and those from El-Badry et al. (2023a). In this case, we obtain $f = 3.9 \pm 0.04 M_{\odot}$,

implying a secondary mass of $9.2 M_{\odot}$ (when the astrometric inclination is included).

4.3. Joint Fits

Our joint fits rely on determining the set of orbits that simultaneously satisfy constraints from both the RV data and the *Gaia* astrometry. We begin with the MCMC chains derived from RVs alone and condition these chains on the *Gaia* astrometry. We achieve this by first choosing random values for parameters unconstrained by RV: parallax, inclination, and position angle of the ascending node. With a random set of these parameters for each step of the chain, we can compute the TI constants and use the *Gaia* DR3 covariance matrix to compute a likelihood. We then re-weight each step of the chain by its corresponding likelihood. In practice, we improve our signal-to-noise ratio by choosing many possible inclinations, position angles, and parallaxes for each step of the RV chain, and computing the *Gaia* likelihood for each of them.

Our conditioning of the RV fits on the *Gaia* covariance matrix immediately reveals a problem. If we adopt the full RV data set — the union of our data and that of El-Badry et al. (2023a) — the goodness-of-fit is formally good for the RVs ($\chi^2 = 24$ for 46 degrees of freedom). The step in this chain that agrees best with *Gaia*, even when freely choosing inclination, position angle, and parallax, has a χ^2 with respect to *Gaia* of 11 with five degrees of freedom. This step is, in turn, a much worse fit to the RVs, with $\Delta\chi^2_{\text{RV}} \approx 12$. The *Gaia* constraint provides an additional five degrees of freedom but increases the total χ^2 by about 20. This would be even worse if the RV errors are underestimated, as suggested by the low χ^2 for the RV-only fit.

The poor formal agreement of *Gaia* astrometry with the RVs renders any resulting confidence intervals dubious. The increases in χ^2 from conditioning on *Gaia* are about a factor of 4 larger what is expected; this suggests that the *Gaia* uncertainties are underestimated by a factor of ≈ 2 . Figure 13 shows this tension in the five parameters constrained both by astrometry and radial velocities; the RV confidence intervals are from the entire RV data set. The 1σ confidence intervals do not overlap in any parameters apart from eccentricity. (We emphasize, though, that both the astrometry and RV data sets independently point to *Gaia* DR3 4373465352415301632 containing a $\sim 10 M_{\odot}$ black hole with a ~ 185 d period. The disagreement discussed here relates only to determining the exact orbital parameters of the system.)

Based on the combined evidence from a satisfactory fit to the RV data and an unsatisfactory joint fit, we inflate the *Gaia* uncertainties by a factor of 2. We re-

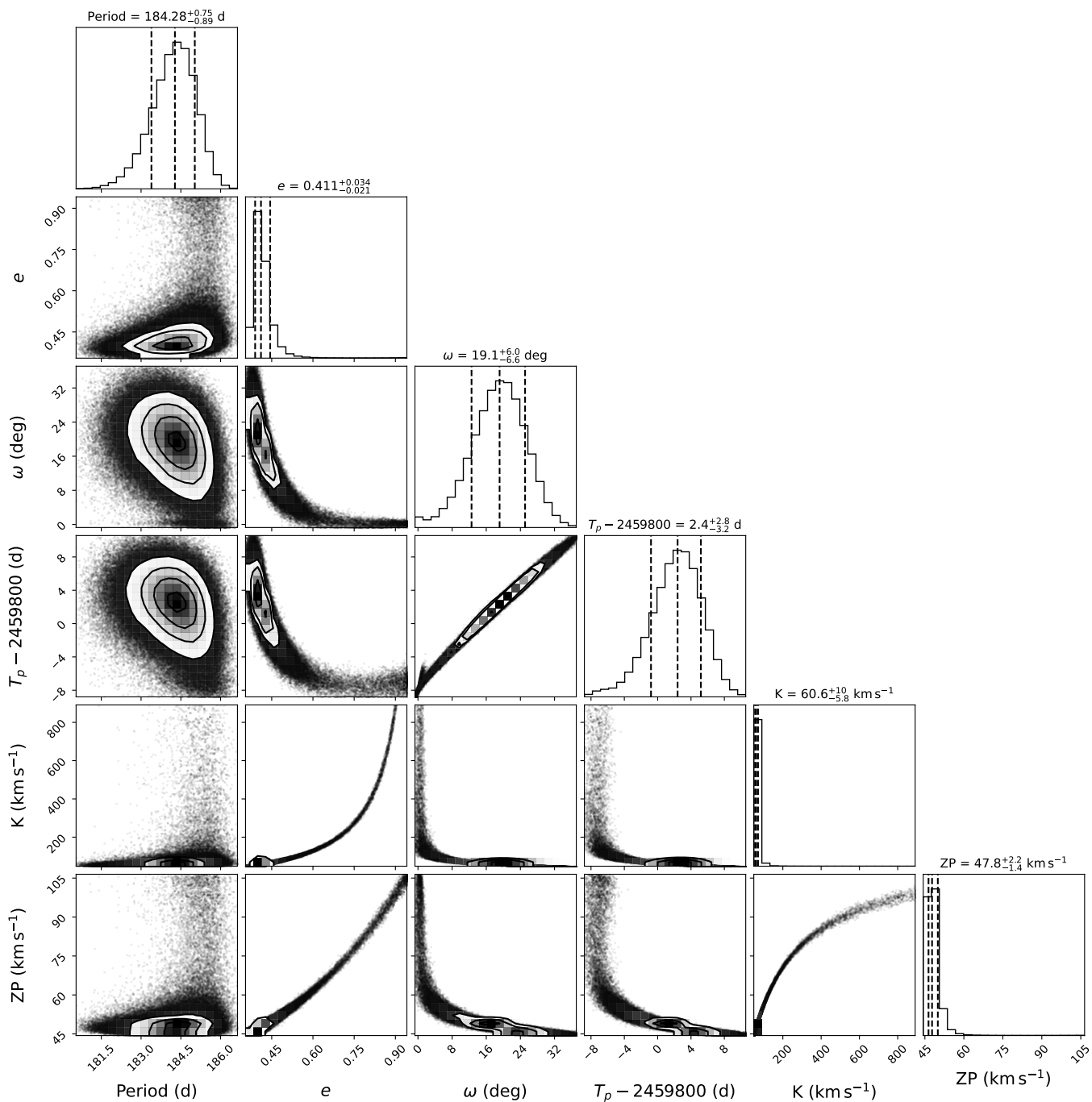


Figure 10. MCMC results for the orbital solution determined from the radial velocity data listed in Table 2, showing only elements in the chain with periods between 175 and 195 days. Although some of the parameters exhibit significant correlations, the overall orbital properties are well constrained by the data, with results similar to those expected from the astrometric solution. Some parameters, like K_1 , do have significant uncertainties.

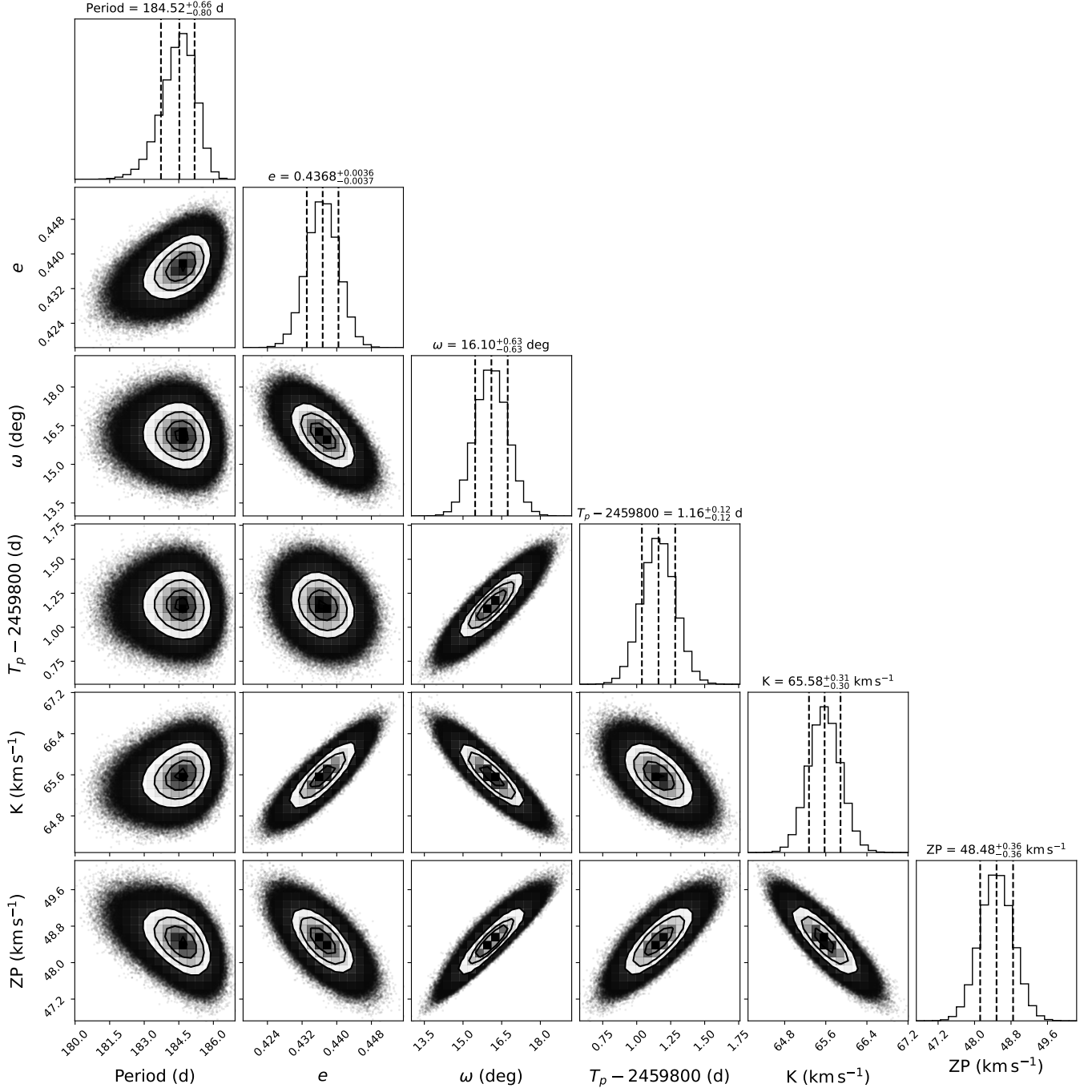


Figure 11. MCMC results for the orbital solution determined from all available radial velocity data, including the measurements from [El-Badry et al. \(2023a\)](#). The orbital solution is much more strongly constrained by the full dataset. We do not show a much sparser cluster of points at $P \approx 218$ d, which contains $\approx 0.4\%$ of the chain.

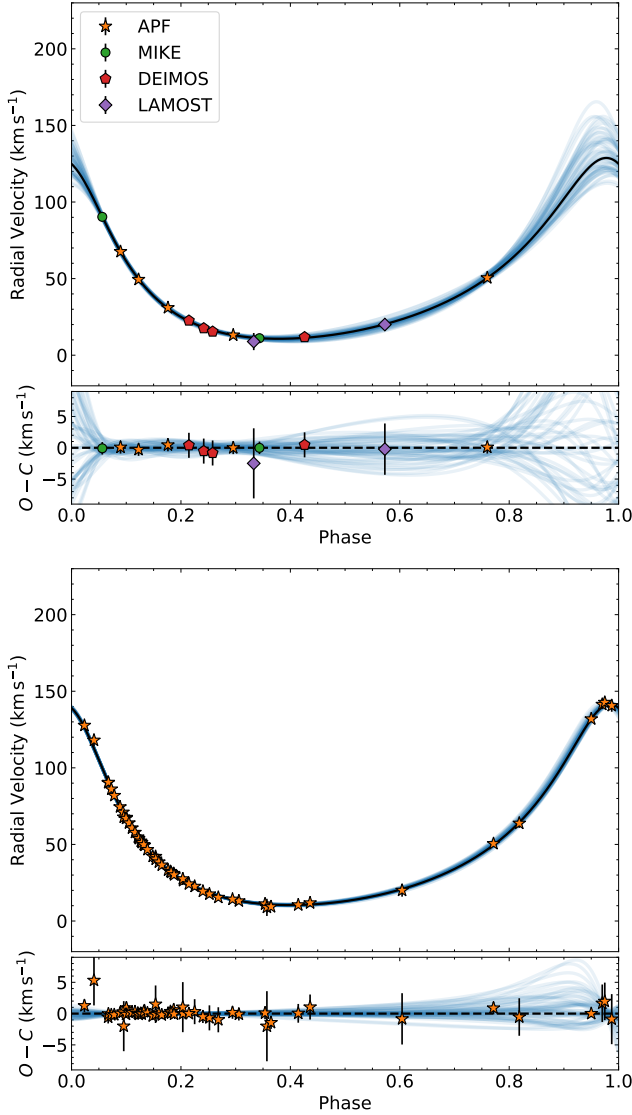


Figure 12. Phase-folded radial velocity curve for the data listed in Table 2 (top) and for all available data (bottom).

The black line in the top panel represents the most likely orbit, and the light blue curves illustrate a random selection of individual MCMC samples. The orbits shown in the top panel are restricted to periods between 175 and 195 days. The residuals, observed minus calculated, are shown in the lower panels. The agreement is within $\sim 5 \text{ km s}^{-1}$ for all RV measurements, and all χ^2 values indicate satisfactory fits, with χ^2 per degree of freedom below 1 for both data sets.

tain the form of the *Gaia* covariance matrix (i.e., the correlation coefficients between parameters) and simply multiply this matrix by a factor of 4. This increase in the uncertainties leads to acceptable joint fits, with χ^2 increasing by ≈ 8 when optimizing the best-fit orbit with the additional five degrees of freedom provided by astrometry.

We therefore adopt the following prescription to condition the RV fits on the *Gaia* astrometry:

- We select many possible sets of random values for parallax, position angle, and inclination for each step in an RV chain;
- We compute the TI constants and evaluate

$$\chi^2 = (\mathbf{p} - \tilde{\mathbf{p}})^T \mathbf{C}_{\text{Gaia}}^{-1} (\mathbf{p} - \tilde{\mathbf{p}}), \quad (2)$$

where \mathbf{p} is the set of parameters from the RV chain (including the additional parameters above), $\tilde{\mathbf{p}}$ are the best-fit *Gaia* values, and \mathbf{C}_{Gaia} is the *Gaia* covariance matrix; and

- We weight each of these steps by $e^{(-\chi^2/8)}$, equivalent to multiplying the *Gaia* covariance matrix by 4 (or doubling the uncertainties). This produces a weighted chain.

Figure 14 presents another way of visualizing the resulting combined constraints and the tension of *Gaia* with the RVs. The top panel shows a random sampling of astrometric orbits compatible with both the union of the RV data sets and the *Gaia* covariance matrix. It is more tightly constrained than the orbits shown in Figure 8 but less so than those shown in El-Badry et al. (2023a) due to our inflation of the *Gaia* uncertainties. We note that El-Badry et al. (2023a) did perform a check with inflated uncertainties but used the published *Gaia* covariance matrix for their baseline case. The lower two panels of Figure 14 show the tension between the astrometry and RVs. The black lines, denoting the steps in the RV chains that best match the *Gaia* astrometry, leave systematics in the RV residuals. This is true both when using only our RVs (middle panel) and using all RVs (lower panel). The light blue lines are randomly drawn from the weighted chains computed as described above. These RV residuals can be compared to those shown in Fig. 12 for the best fit to the RVs alone.

Our joint constraints for *Gaia* DR3 4373465352415301632 using both our radial velocity data and the astrometry are listed in Table 6 (which also provides the astrometric fit and posteriors that result from fitting to the velocities only). Figure 15 displays the resultant corner plot for the derived parameters of the combined fit using the RV data listed in Table 2. We find that the secondary mass of *Gaia* DR3 4373465352415301632 is $11.64^{+1.52}_{-1.31} M_{\odot}$. Using all of the available radial velocity data gives the posterior distributions shown in Figure 16 and parameters listed in the bottom section of Table 7, leading to a smaller secondary mass of $9.326^{+0.216}_{-0.209} M_{\odot}$ that is in closer agreement with El-Badry et al. (2023a).

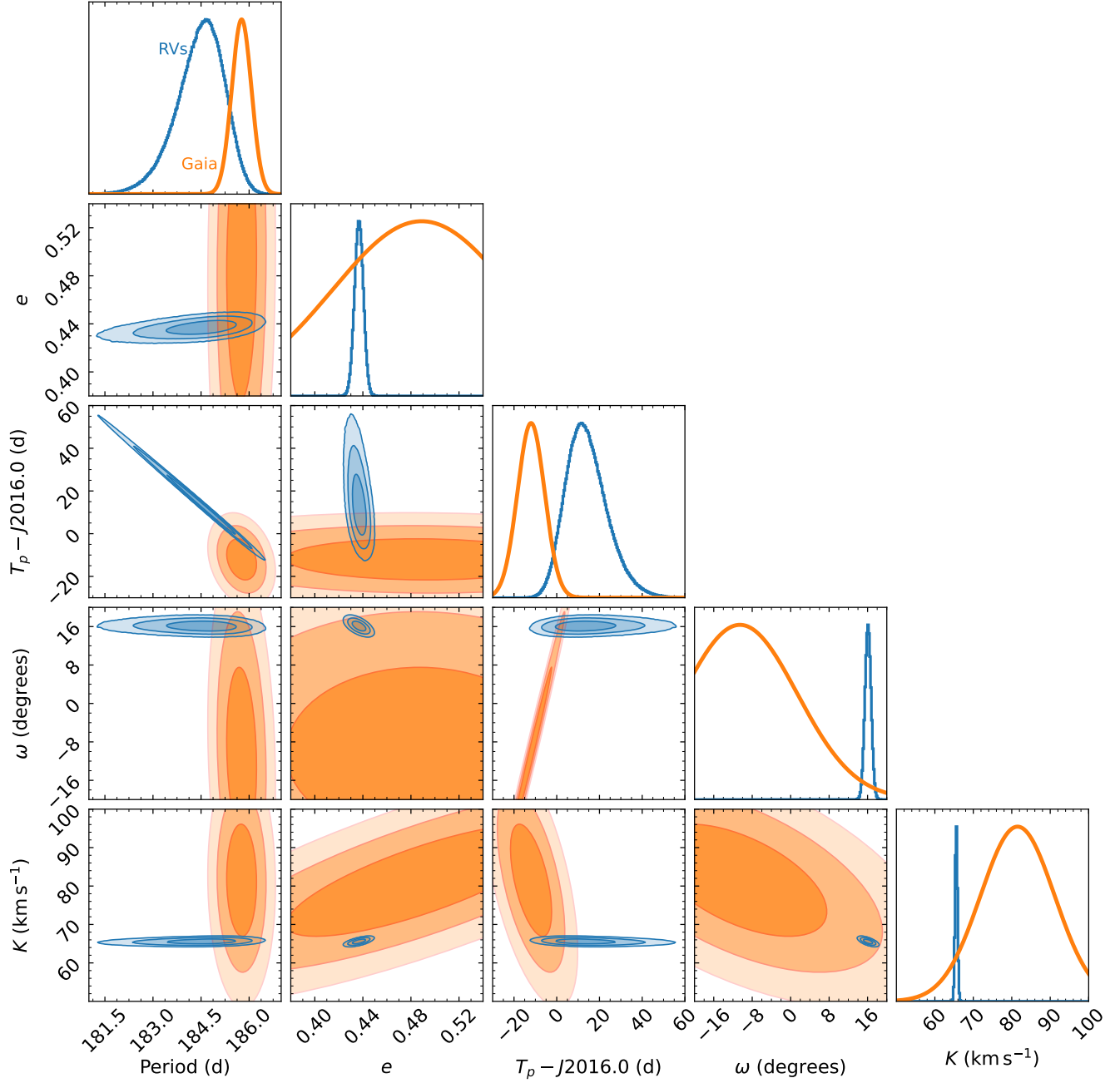


Figure 13. 1-, 2- and 3- σ confidence levels resulting from fits to all available RV data (blue contours), compared to the reported constraints from *Gaia* astrometry (orange contours). Although the RV data are qualitatively consistent with the *Gaia* astrometry, most orbital parameters show discrepancies at the 2-3 σ level even with the full RV dataset. Since the χ^2 value for RV fits indicates that the velocity uncertainties have not been underestimated, we conclude that the *Gaia* errors must have been underestimated.

5. DISCUSSION

As noted in Section 1, during the preparation of this manuscript, on 2022 September 14 [El-Badry et al. \(2023a\)](#) submitted to MNRAS and posted a preprint of an analysis of this same source selected from the *Gaia* DR3 catalog. The overall conclusions of the two studies are in good agreement, that the spectroscopic and astrometric measurements of *Gaia* DR3 4373465352415301632 both independently and together demonstrate that the companion is a massive black hole. [El-Badry et al. \(2023a\)](#) have a much more accurate RV-only solution due to their extensive RV coverage. Based on our joint fits to our RV data and astrometry, we infer a companion mass of $11.64^{+1.52}_{-1.31} M_{\odot}$, whereas [El-Badry et al. \(2023a\)](#) report a lower companion mass of $9.62 \pm 0.18 M_{\odot}$. As noted earlier, our observations did not cover the peak of the radial velocity curve, limiting the precision with which we can determine the velocity semi-amplitude of the primary. Consequently, the best-fit peak-to-trough amplitude of the orbital solution using our RV data is $\sim 160 \text{ km s}^{-1}$, compared to $\sim 140 \text{ km s}^{-1}$ in [El-Badry et al. \(2023a\)](#). As discussed in §4, the combination of both data sets allows us to derive an unimodal solution for the orbital period, independent of *Gaia*'s astrometric solution. The joint fit to all available RV data and the astrometry yields the most accurate solution thus far.

5.1. Comparison with Theoretical Predictions

Prior to *Gaia* DR3, several studies calculated the expected population of black holes with luminous companions that could be detected with *Gaia*. The predicted *Gaia* yields range from tens to thousands of such binaries by the end of the mission ([Breivik et al. 2017](#); [Mashian & Loeb 2017](#); [Wiktorowicz et al. 2020](#); [Chawla et al. 2022](#); [Shikauchi et al. 2022](#); [Wang et al. 2022](#); [Janssens et al. 2022](#)). Although the quality cuts on orbital solutions described by [Halbwachs et al. \(2022\)](#) may have removed more binary systems that contain black holes, the identification of only two confident black hole-luminous companion binaries in DR3 so far (see [El-Badry et al. \(2023b\)](#), as well as the earlier identification of this source by [Tanikawa et al. \(2022\)](#) in their analysis of *Gaia* data) suggests that the upper end of those predictions is likely too optimistic. The properties of *Gaia* DR3 4373465352415301632 are quite similar to the most common binary parameters predicted by, e.g., [Breivik et al. \(2017\)](#), [Yalinewich et al. \(2018\)](#), and [Shao & Li \(2019\)](#) in black hole mass, companion mass, period, semi-major axis, and apparent magnitude. The only deviation from those expectations is the eccentricity, where the observed value differs from the most likely values of

$e < 0.1$ or (in the case of significant kick velocities) $e > 0.9$. Below we speculate that the observed eccentricity of $e \sim 0.4$ may have resulted from a possible architecture of a hierarchical triple system. Stellar triples are a common architecture and can affect the dynamical evolution of the system ([Vigna-Gómez et al. 2022](#); [Tokovinin et al. 2006](#); [Tokovinin & Moe 2020](#); [Lennon et al. 2022](#); [Chakrabarti et al. 2022](#)).

5.2. Formation Scenarios

Although the characteristics of the *Gaia* DR3 4373465352415301632 binary system do not appear to be unusual with respect to population synthesis predictions for binaries detectable by *Gaia*, the particular combination of properties we have determined may require fine-tuning to explain. To begin with, the mass ratio of the system is quite large, $M_2/M_1 = 10.3 \pm 1.2$. Although some low-mass companions to massive stars have been identified (e.g., [GRAVITY Collaboration et al. 2018](#); [Reggiani et al. 2022c](#)), this does not seem to be the most common configuration for OB stars. The initial mass ratio of the system must have been even larger; the initial-final mass relation of [Raitzel et al. \(2018\)](#) suggests that a $\sim 10 M_{\odot}$ black hole would have had a zero age main sequence mass of $\sim 15\text{--}50 M_{\odot}$. Moreover, it is not clear that a binary with a separation of $\sim 1 \text{ AU}$ should have survived the evolution of the massive component. Prior to the formation of the black hole, the orbit must have been tighter because of the mass that the system lost when the black hole formed. (If the black hole received a natal kick, that also would have heated the system, further reducing the inferred initial separation.) The maximum radius reached by a $15\text{--}50 M_{\odot}$ star after crossing the Hertzsprung gap is $\gtrsim 400 R_{\odot}$ ([Martins & Palacios 2013](#)), indicating that the system could not have avoided a common envelope phase, unless the progenitor evolved quasi-homogeneously (e.g., [El-Badry et al. 2022b](#); [Ramachandran et al. 2019](#); [Gilkis et al. 2021](#), suggesting that stars more massive than $\sim 30 M_{\odot}$ may evolve quasi-homogeneously without respect to rotation.) Depending on the duration of that period and on the common envelope ejection efficiency, a merger might be expected to follow, making the survival of the G star until the present surprising.

One way to avoid this conundrum is if the system was initially a triple, consisting of an inner binary orbited by the G star. Massive stars are often found with close massive companions ([Sana et al. 2012](#)), so there would be nothing unusual about this architecture. Interactions between the two inner stars could then have proceeded either via mass loss or a merger in such a way as to prevent either star from expanding enough to en-

gulf their wider companion. The question posed by this scenario is whether the inner binary ultimately merged, either before or after the formation of the black hole. If so, that merger could have resulted in the production of the $9.3 M_{\odot}$ black hole we have identified. On the other hand, if the stars did not merge, an inner binary of two compact objects with a combined mass of $9.3 M_{\odot}$ could still be present. Many such combinations are possible, and of course this suggestion is entirely speculative at the moment, but a binary with a combined mass of $9.3 M_{\odot}$ would likely involve at least one object residing in the mass gap (e.g., Özel et al. 2010), which would be of considerable interest. In the next section, we discuss whether there would be any observable consequences of the $9.3 M_{\odot}$ dark mass being subdivided into a binary.

5.3. A Third Companion?

We have investigated with `orvara` the possibility that *Gaia* DR3 4373465352415301632 may be a triple system containing two unseen companions, but our present data set does not allow us to constrain the posterior distributions of a hierarchical triple. Extended radial velocity monitoring could make it possible to study the rich dynamics of a triple system, and we briefly speculate here on some of the possibilities that could be directly observed. Although the incidence of triples drops dramatically for periods greater than ~ 10 days (Tokovinin et al. 2006; Tokovinin & Moe 2020), compact triple systems are not uncommon, and indeed in eclipsing binaries, there is a population of compact triples that manifest large eclipse transit variations (Borkovits et al. 2015). Here, we focus on the more likely possibility of a compact inner binary with the G star as part of the outer system (Section 5.2). A similar scenario has been investigated in El-Badry et al. (2023a).

If this indeed is a hierarchical triple system, the Kozai-Lidov mechanism would allow for an exchange between the eccentricity and the inclination (Chang 2009; Naoz et al. 2013; Suzuki et al. 2019). The Kozai-Lidov timescale (Antognini 2015), t_{KL} , is given by:

$$t_{\text{KL}} \sim P_{\text{in}} \frac{m_1 + m_2}{m_3} \left(\frac{a_{\text{out}}}{a_{\text{in}}} \right)^3 (1 - e_{\text{out}}^2)^{3/2}, \quad (3)$$

where P_{in} is the orbital period of the inner binary, a_{out} and a_{in} are the semi-major axes of the outer and inner systems, e_{out} is the eccentricity of the outer system, and the masses of the three bodies are given by m_1, m_2 and m_3 . For our specific case here, if we consider an inner binary of combined mass $m_1 + m_2 \sim 9.3 M_{\odot}$ that has a third body with a semimajor axis that is 3(10) times that of the inner binary, this gives a Kozai-Lidov timescale of $\sim 100(5000)$ years. However, the shift in

the velocity is $\sim 10^{-2}(10^{-4})$ per orbital period. For this specific case, the velocity change in physical units translates to $\sim 1000(10)$ m s $^{-1}$ per orbit, which could in principle be observed, especially if the inner binary is not too close. This effect (the osculation of the orbit of the inner binary due to the Kozai-Lidov effect) is modified by a general relativistic correction term (Anderson et al. 2017). This is likely the dominant dynamical effect beyond that of Keplerian motion. Other dynamical effects for binary systems recently reviewed by Chakrabarti et al. (2022) (including tidal effects and the general relativistic precession) are sub-dominant to this signal. Thus, the effects of the Kozai-Lidov effect may become manifest over several orbital periods for this system even for a widely separated hierarchical system. In this context, it is advantageous that the companion star is a G star, with spectra that indicate that it has low stellar jitter (Wright 2005). For stars with low stellar jitter, high precision measurements should be able to capture this effect.

5.4. Comparison with 2MASS J05215658+4359220

Earlier work on the report of the black hole binary system with a non-interacting giant companion by Thompson et al. (2019) indicated an unusually high [C/N] abundance ratio for its mass and evolutionary state. If the mass inferred for the red giant is correct, this abundance pattern may have resulted from previous interaction with the black hole progenitor star (we note that van den Heuvel & Tauris (2020b) argue that if the red giant’s mass is $\sim 1 M_{\odot}$, the companion could be a binary with two main-sequence stars). Low-mass X-ray binaries with black hole companions are also found to be metal rich, with large abundances of α elements (Casares et al. 2017). For *Gaia* DR3 4373465352415301632, a comparison with synthetic spectra indicates an approximately solar [C/N] ratio, as expected for a main sequence star of its metallicity. The [C/N] ratio of *Gaia* DR3 4373465352415301632 places it in the typical observed locus of main-sequence stars (Pinsonneault et al. 2018), consistent with its small Roche lobe to semi-major axis ratio; we find that the Roche limit to the semi-major axis for the G star is 0.2, indicating that it is stable against tidal disintegration.

5.5. Estimate for the Number of Systems in the Galaxy

Given the current uncertainty in the formulation of the common envelope channel, we adopt a simpler approach and estimate the number of such systems that may exist in the Galaxy. Here, we do not consider binary (and triple) evolution effects, which may be more significant than IMF dependencies. We assume a Salpeter

IMF:

$$\frac{dn}{dm} = \mathcal{N}m^{-2.35}, \quad (4)$$

where dn/dm is the number of stars per mass bin, and the normalization, \mathcal{N} , can be set by integrating the number of stars per mass bin over the limits of the masses of stars in the Salpeter IMF, i.e., where $m_{\min} = 0.1 M_{\odot}$ and $m_{\max} = 100 M_{\odot}$ are the upper and lower limits, and equating to the observed number of stars in the Galaxy, N_* . The binary fraction of high mass stars is nearly unity ($f_b \sim 1$) (Sana et al. 2009; Maíz Apellániz et al. 2016) and the companion masses, m_c , are taken from a flat distribution in mass ratio, $q = m_c/m$, e.g., $dP/dq = 1$ (Sana et al. 2012; Chulkov 2021).

$$\begin{aligned} N &= f_b \mathcal{N} \int_{m_{\text{lower}}}^{m_{\text{max}}} \frac{dn}{dm} dm \int_{q_1}^{q_2} \frac{dP}{dq} dq \\ &= 0.42 f_b \mathcal{N} (m_{\text{lower}}^{-2.35} - m_{\text{max}}^{-2.35}) (m_2 - m_1) \end{aligned} \quad (5)$$

where m_{lower} is the minimum progenitor mass required to form a $\sim 10 M_{\odot}$ black hole, which we take to be $\sim 20 M_{\odot}$ (Sukhbold et al. 2016) and m_1 and m_2 are the lower and upper mass range of zero-age main sequence masses of G-type stars, which we take to be $0.8 M_{\odot}$ and $1.2 M_{\odot}$. This gives a total number of binaries of $\sim 8 \times 10^5$, which is comparable to the number of binaries with a black hole and a luminous companion in the zero-kick model by Breivik et al. (2017).

5.6. Milky Way Orbit

We integrate the orbit of *Gaia* DR3 4373465352415301632 backwards in time 500 Myr in the Galactic potential, as shown in Figure 17. Here, we use the potential derived from accelerations measured directly from pulsar timing (Chakrabarti et al. 2021), which provides the most direct probe of the Galactic mass distribution. Using potentials derived from kinematic assumptions (e.g., Bovy 2015) produces similar results to within a factor of ~ 2 . The star remains confined within a few hundred pc of the Galactic plane at all times, confirming that it formed as part of the thin disk population. Unless the natal kick of the black hole happened to be oriented within the disk of the Galaxy, the low scale height of the orbit indicates that the kick velocity must have been small. Given the low scale height of the orbit, ~ 0.4 kpc, the vertical kick velocity is of order ~ 10 km/s. This is similar to the negligible kick velocities for Cyg X-1 and VFTS 243 (Mirabel & Rodrigues 2003; Shenar et al. 2022). The orbit of *Gaia* DR3 4373465352415301632 around the Milky Way is somewhat eccentric, with a pericenter of ~ 7 kpc and apocenter of ~ 12 kpc, reaching sub-

stantially larger distances than the Sun does, consistent with its older age.

6. CONCLUSION

We summarize below our main results:

- We searched the *Gaia* DR3 binary catalog to identify possible black hole companions to main sequence stars. We identified *Gaia* DR3 4373465352415301632 as a particularly interesting source on the basis of its large mass ratio and location near the *Gaia* main sequence.
- Fitting the SED of *Gaia* DR3 4373465352415301632 with single stellar atmosphere models, we find that the photometry is consistent with a modestly metal-poor G star on the main sequence. Adding a second source does not substantially improve the quality of the SED fits, indicating no evidence for the presence of more than one luminous star.
- We determine stellar parameters from a high-resolution spectrum, finding $T_{\text{eff}} = 5972 \pm 100$ K, $\log g = 4.54 \pm 0.15$, $[\text{Fe}/\text{H}] = -0.30 \pm 0.10$, $M = 0.91 \pm 0.10 M_{\odot}$, and age = 7.1 ± 3.8 Gyr, which are generally in good agreement with those inferred from the SED. The chemical abundance pattern shows no abnormalities compared to other stars with similar metallicities, and the spectrum contains lines from only one star.
- We have carried out follow-up radial velocity observations for this source over the four months from its discovery until it went into conjunction with the Sun, and our fits to the velocities give an orbital period of $184.28^{+0.75}_{-0.89}$ d, an eccentricity of $0.411^{+0.034}_{-0.021}$, and a velocity semi-amplitude of $60.6^{+10.0}_{-5.8}$ km s $^{-1}$. The radial velocity curve predicted from the astrometric orbital solution is in reasonable agreement with the data, confirming that the *Gaia* orbit is not spurious. We then computed joint fits to the astrometric data and the RVs, which (including the RV measurements from El-Badry et al. 2023a) give a companion mass of $9.326^{+0.216}_{-0.209} M_{\odot}$, an orbital period of $185.52^{+0.08}_{-0.08}$ d, an eccentricity of $0.439^{+0.0036}_{-0.0030}$, a semi-major axis of $1.258^{+0.010}_{-0.011}$ AU, and an inclination of $126^{\circ}79 \pm 0^{\circ}62$.
- The fit to all available RV data gives a best-fit χ^2 of 24 for 52 total radial velocity measurements and six free parameters (46 degrees of freedom). This low χ^2 value indicates the RV errors and our derived parameter uncertainties may be overestimated. However, there is $\sim 2\sigma$ disagreement between the best-fit parameters from the RVs and the *Gaia* astrometry. The 1-sigma confidence intervals overlap only for the eccentricity. For our joint fits to the astrometry and RV data, we find that when we condition the RV fits on the *Gaia* data, the increase in χ^2 is a factor of four greater than what is ex-

pected, which suggests the *Gaia* uncertainties have been underestimated by a factor of ≈ 2 .

- Given the combination of the large mass of the dark companion and a semi-major axis of *Gaia* DR3 4373465352415301632 that is neither very large nor very small, the formation channel for this system is not immediately clear. However, the most natural scenario may be that the visible G star was originally the outer tertiary component orbiting a close inner binary with two massive stars. A similar possibility is also discussed in El-Badry et al. (2023a).

- The orbit of this system in the Galaxy is consistent with that of thin disk stars, and the low scale height of the integrated Galactic orbit indicates that the kick velocity must have been small. At a distance of 468 ± 4 pc after correcting for the DR3 parallax bias (Lindgren et al. 2021b), as discussed by El-Badry et al. (2023a), *Gaia* DR3 4373465352415301632 is closer to the Sun than any black hole X-ray binaries with known distances (Corral-Santana et al. 2016) or any of the black holes identified through other techniques (Thompson et al. 2019; Lam et al. 2022; Sahu et al. 2022).

- Discoveries of black holes around luminous stars from their measured accelerations now provide a new avenue for understanding the formation channels of black holes in the Galaxy. Simple estimates suggest that there are $\sim 10^6$ similar systems in the Milky Way. Although our current data cannot constrain the possibility that *Gaia* DR3 4373465352415301632 is actually a triple, future RV monitoring may enable us to witness the rich dynamics that can be manifest in hierarchical triple systems.

1 We thank the anonymous referee for a thorough review
2 that helped improve the paper. We are grateful to Mirek
3 Brandt for helpful discussions on *orvara*, Adrian Price-
4 Whelan for assistance with *The Joker*, Brad Holden for
5 his help with APF data and observations, Lieke van Son
6 for discussion of binary evolution, and Alex Ji for advice
7 on MIKE data handling in Python. SC also acknowl-
8 edges support from NSF AAG 2009828 and from the
9 RCSA time domain astrophysics program.

10 This work has made use of data from the Euro-
11 pean Space Agency (ESA) mission *Gaia* (<https://www.cosmos.esa.int/gaia>),
12 processed by the *Gaia* Data Pro-
13 cessing and Analysis Consortium (DPAC, <https://www.cosmos.esa.int/web/gaia/dpac/consortium>).
14 Funding for the DPAC has been provided by national institu-
15 tions, in particular the institutions participating in the
16 *Gaia* Multilateral Agreement.

17 This paper includes data gathered with the 6.5 meter
18 Magellan Telescopes located at Las Campanas Observa-
19 tory, Chile.

20 Some of the data presented herein were obtained at the
21 W. M. Keck Observatory, which is operated as a scien-
22 tific partnership among the California Institute of Tech-
23 nology, the University of California and the National
24 Aeronautics and Space Administration. The Observa-
25 tory was made possible by the generous financial sup-
26 port of the W. M. Keck Foundation. The authors wish
27 to recognize and acknowledge the very significant cul-
28 tural role and reverence that the summit of Maunakea
29 has always had within the indigenous Hawaiian commu-
30 nity. We are most fortunate to have the opportunity to
31 conduct observations from this mountain.

32 Guoshoujing Telescope (the Large Sky Area Multi-
33 Object Fiber Spectroscopic Telescope LAMOST) is a
34 National Major Scientific Project built by the Chinese
35 Academy of Sciences. Funding for the project has
36 been provided by the National Development and Reform
37 Commission. LAMOST is operated and managed by the
38 National Astronomical Observatories, Chinese Academy
39 of Sciences.

40 This research has made use of NASA’s Astrophysics
41 Data System Bibliographic Services.

Facilities:

Facility: *Gaia*, Magellan:II (MIKE), Automated Planet Finder (Levy), Keck:II (DEIMOS)

Software:

Software: ARIADNE (Vines & Jenkins 2022), SpecMatch-Emp (Yee et al. 2017), smhr (Casey 2014), isochrones (Morton 2015), MultiNest (Feroz & Hobson 2008; Feroz et al. 2009, 2019), PyMultinest (Buchner

et al. 2014), MOOG (Snedden 1973), orvara (Brandt et al.

2021), *The Joker* (Price-Whelan et al. 2017), exoplanet (Foreman-Mackey et al. 2021a,b)

REFERENCES

- Abbott, B. P., Abbott, R., Abbott, T. D., et al. 2016, *PhRvD*, 93, 122003, doi: [10.1103/PhysRevD.93.122003](https://doi.org/10.1103/PhysRevD.93.122003)
- . 2019, *ApJL*, 882, L24, doi: [10.3847/2041-8213/ab3800](https://doi.org/10.3847/2041-8213/ab3800)
- Abbott, R., Abbott, T. D., Abraham, S., et al. 2021, *Physical Review X*, 11, 021053, doi: [10.1103/PhysRevX.11.021053](https://doi.org/10.1103/PhysRevX.11.021053)
- Abdul-Masih, M., Banyard, G., Bodensteiner, J., et al. 2020, *Nature*, 580, E11, doi: [10.1038/s41586-020-2216-x](https://doi.org/10.1038/s41586-020-2216-x)
- Ahumada, R., Prieto, C. A., Almeida, A., et al. 2020, *ApJS*, 249, 3, doi: [10.3847/1538-4365/ab929e](https://doi.org/10.3847/1538-4365/ab929e)
- Amarsi, A. M., & Asplund, M. 2017, *MNRAS*, 464, 264, doi: [10.1093/mnras/stw2445](https://doi.org/10.1093/mnras/stw2445)
- Amarsi, A. M., Lind, K., Asplund, M., Barklem, P. S., & Collet, R. 2016, *MNRAS*, 463, 1518, doi: [10.1093/mnras/stw2077](https://doi.org/10.1093/mnras/stw2077)
- Amarsi, A. M., Nissen, P. E., & Skúladóttir, Á. 2019, *A&A*, 630, A104, doi: [10.1051/0004-6361/201936265](https://doi.org/10.1051/0004-6361/201936265)
- Amarsi, A. M., Lind, K., Osorio, Y., et al. 2020, *A&A*, 642, A62, doi: [10.1051/0004-6361/202038650](https://doi.org/10.1051/0004-6361/202038650)
- Anderson, K. R., Lai, D., & Storch, N. I. 2017, *MNRAS*, 467, 3066, doi: [10.1093/mnras/stx293](https://doi.org/10.1093/mnras/stx293)
- Andrews, J. J., Taggart, K., & Foley, R. 2022, arXiv e-prints, arXiv:2207.00680. <https://arxiv.org/abs/2207.00680>
- Antonini, F., & Rasio, F. A. 2016, *ApJ*, 831, 187, doi: [10.3847/0004-637X/831/2/187](https://doi.org/10.3847/0004-637X/831/2/187)
- Asplund, M., Amarsi, A. M., & Grevesse, N. 2021, *A&A*, 653, A141, doi: [10.1051/0004-6361/202140445](https://doi.org/10.1051/0004-6361/202140445)
- Bavera, S. S., Fragos, T., Qin, Y., et al. 2020, *A&A*, 635, A97, doi: [10.1051/0004-6361/201936204](https://doi.org/10.1051/0004-6361/201936204)
- Belczynski, K., Holz, D. E., Bulik, T., & O’Shaughnessy, R. 2016, *Nature*, 534, 512, doi: [10.1038/nature18322](https://doi.org/10.1038/nature18322)
- Berg, D. A., Pogge, R. W., Skillman, E. D., et al. 2020, *ApJ*, 893, 96, doi: [10.3847/1538-4357/ab7eab](https://doi.org/10.3847/1538-4357/ab7eab)
- Bernstein, R., Shtetman, S. A., Gunnels, S. M., Mochmacki, S., & Athey, A. E. 2003, in *Society of Photo-Optical Instrumentation Engineers (SPIE) Conference Series*, Vol. 4841, Instrument Design and Performance for Optical/Infrared Ground-based Telescopes, ed. M. Iye & A. F. M. Moorwood, 1694–1704, doi: [10.1117/12.461502](https://doi.org/10.1117/12.461502)
- Binnendijk, L. 1960, Properties of double stars; a survey of parallaxes and orbits.
- Blackwell-Whitehead, R. J., Toner, A., Hibbert, A., Webb, J., & Ivarsson, S. 2005, *MNRAS*, 364, 705, doi: [10.1111/j.1365-2966.2005.09597.x](https://doi.org/10.1111/j.1365-2966.2005.09597.x)
- Bodensteiner, J., Shenar, T., Mahy, L., et al. 2020, *A&A*, 641, A43, doi: [10.1051/0004-6361/202038682](https://doi.org/10.1051/0004-6361/202038682)
- Borkovits, T., Rappaport, S., Hajdu, T., & Sztakovics, J. 2015, *MNRAS*, 448, 946, doi: [10.1093/mnras/stv015](https://doi.org/10.1093/mnras/stv015)
- Bovy, J. 2015, *ApJS*, 216, 29, doi: [10.1088/0067-0049/216/2/29](https://doi.org/10.1088/0067-0049/216/2/29)
- Brandt, T. D., Dupuy, T. J., Li, Y., et al. 2021, *AJ*, 162, 186, doi: [10.3847/1538-3881/ac042e](https://doi.org/10.3847/1538-3881/ac042e)
- Breivik, K., Chatterjee, S., & Larson, S. L. 2017, *ApJL*, 850, L13, doi: [10.3847/2041-8213/aa97d5](https://doi.org/10.3847/2041-8213/aa97d5)
- Bresolin, F., Kennicutt, R. C., & Ryan-Weber, E. 2012, *ApJ*, 750, 122, doi: [10.1088/0004-637X/750/2/122](https://doi.org/10.1088/0004-637X/750/2/122)
- Brewer, J. M., Fischer, D. A., Valenti, J. A., & Piskunov, N. 2016, *ApJS*, 225, 32, doi: [10.3847/0067-0049/225/2/32](https://doi.org/10.3847/0067-0049/225/2/32)
- Buchner, J., Georgakakis, A., Nandra, K., et al. 2014, *A&A*, 564, A125, doi: [10.1051/0004-6361/201322971](https://doi.org/10.1051/0004-6361/201322971)
- Butler, R. P., Marcy, G. W., Williams, E., et al. 1996, *PASP*, 108, 500, doi: [10.1086/133755](https://doi.org/10.1086/133755)
- Capitanio, L., Lallement, R., Vergely, J. L., Elyajouri, M., & Monreal-Ibero, A. 2017, *A&A*, 606, A65, doi: [10.1051/0004-6361/201730831](https://doi.org/10.1051/0004-6361/201730831)
- Casali, G., Spina, L., Magrini, L., et al. 2020, *A&A*, 639, A127, doi: [10.1051/0004-6361/202038055](https://doi.org/10.1051/0004-6361/202038055)
- Casares, J., Jonker, P. G., & Israelian, G. 2017, in *Handbook of Supernovae*, ed. A. W. Alsabti & P. Murdin, 1499, doi: [10.1007/978-3-319-21846-5_111](https://doi.org/10.1007/978-3-319-21846-5_111)
- Casey, A. R. 2014, PhD thesis, Australian National University, Canberra
- Castelli, F., & Kurucz, R. L. 2003, in *Modelling of Stellar Atmospheres*, ed. N. Piskunov, W. W. Weiss, & D. F. Gray, Vol. 210, A20. <https://arxiv.org/abs/astro-ph/0405087>
- Chakrabarti, S., Chang, P., Lam, M. T., Vigeland, S. J., & Quillen, A. C. 2021, *ApJL*, 907, L26, doi: [10.3847/2041-8213/abd635](https://doi.org/10.3847/2041-8213/abd635)
- Chakrabarti, S., Chang, P., O’Shaughnessy, R., et al. 2017, *ApJL*, 850, L4, doi: [10.3847/2041-8213/aa9655](https://doi.org/10.3847/2041-8213/aa9655)
- Chakrabarti, S., Dell, B., Graur, O., et al. 2018, *ApJL*, 863, L1, doi: [10.3847/2041-8213/aad0a4](https://doi.org/10.3847/2041-8213/aad0a4)
- Chakrabarti, S., Stevens, D. J., Wright, J., et al. 2022, *ApJL*, 928, L17, doi: [10.3847/2041-8213/ac5c43](https://doi.org/10.3847/2041-8213/ac5c43)
- Chang, P. 2009, *MNRAS*, 393, 224, doi: [10.1111/j.1365-2966.2008.14202.x](https://doi.org/10.1111/j.1365-2966.2008.14202.x)
- Chawla, C., Chatterjee, S., Breivik, K., et al. 2022, *ApJ*, 931, 107, doi: [10.3847/1538-4357/ac60a5](https://doi.org/10.3847/1538-4357/ac60a5)

- Choi, J., Dotter, A., Conroy, C., et al. 2016, *ApJ*, 823, 102, doi: [10.3847/0004-637X/823/2/102](https://doi.org/10.3847/0004-637X/823/2/102)
- Chubak, C., Marcy, G., Fischer, D. A., et al. 2012, arXiv e-prints, arXiv:1207.6212. <https://arxiv.org/abs/1207.6212>
- Chulkov, D. 2021, *MNRAS*, 501, 769, doi: [10.1093/mnras/staa3601](https://doi.org/10.1093/mnras/staa3601)
- Cooper, M. C., Newman, J. A., Davis, M., Finkbeiner, D. P., & Gerke, B. F. 2012, spec2d: DEEP2 DEIMOS Spectral Pipeline, Astrophysics Source Code Library, record ascl:1203.003. <http://ascl.net/1203.003>
- Corral-Santana, J. M., Casares, J., Muñoz-Darias, T., et al. 2016, *A&A*, 587, A61, doi: [10.1051/0004-6361/201527130](https://doi.org/10.1051/0004-6361/201527130)
- . 2013, *Science*, 339, 1048, doi: [10.1126/science.1228222](https://doi.org/10.1126/science.1228222)
- Cui, X.-Q., Zhao, Y.-H., Chu, Y.-Q., et al. 2012, *Research in Astronomy and Astrophysics*, 12, 1197, doi: [10.1088/1674-4527/12/9/003](https://doi.org/10.1088/1674-4527/12/9/003)
- Cutri, R. M., Skrutskie, M. F., van Dyk, S., et al. 2003, 2MASS All Sky Catalog of point sources.
- Cutri, R. M., Wright, E. L., Conrow, T., et al. 2021, *VizieR Online Data Catalog*, II/328
- de Mink, S. E., & Mandel, I. 2016, *MNRAS*, 460, 3545, doi: [10.1093/mnras/stw1219](https://doi.org/10.1093/mnras/stw1219)
- Dotter, A. 2016, *ApJS*, 222, 8, doi: [10.3847/0067-0049/222/1/8](https://doi.org/10.3847/0067-0049/222/1/8)
- El-Badry, K., & Burdge, K. B. 2022, *MNRAS*, 511, 24, doi: [10.1093/mnrasl/slab135](https://doi.org/10.1093/mnrasl/slab135)
- El-Badry, K., Burdge, K. B., & Mróz, P. 2022a, *MNRAS*, 511, 3089, doi: [10.1093/mnras/stac274](https://doi.org/10.1093/mnras/stac274)
- El-Badry, K., Conroy, C., Fuller, J., et al. 2022b, *MNRAS*, 517, 4916, doi: [10.1093/mnras/stac2945](https://doi.org/10.1093/mnras/stac2945)
- El-Badry, K., & Quataert, E. 2020, *MNRAS*, 493, L22, doi: [10.1093/mnrasl/slaa004](https://doi.org/10.1093/mnrasl/slaa004)
- . 2021, *MNRAS*, 502, 3436, doi: [10.1093/mnras/stab285](https://doi.org/10.1093/mnras/stab285)
- El-Badry, K., & Rix, H.-W. 2022, *MNRAS*, 515, 1266, doi: [10.1093/mnras/stac1797](https://doi.org/10.1093/mnras/stac1797)
- El-Badry, K., Seeburger, R., Jayasinghe, T., et al. 2022c, *MNRAS*, 512, 5620, doi: [10.1093/mnras/stac815](https://doi.org/10.1093/mnras/stac815)
- El-Badry, K., Rix, H.-W., Quataert, E., et al. 2023a, *MNRAS*, 518, 1057, doi: [10.1093/mnras/stac3140](https://doi.org/10.1093/mnras/stac3140)
- El-Badry, K., Rix, H.-W., Cendes, Y., et al. 2023b, arXiv e-prints, arXiv:2302.07880, doi: [10.48550/arXiv.2302.07880](https://doi.org/10.48550/arXiv.2302.07880)
- Eldridge, J. J., Stanway, E. R., Breivik, K., et al. 2020, *MNRAS*, 495, 2786, doi: [10.1093/mnras/staa1324](https://doi.org/10.1093/mnras/staa1324)
- Faber, S. M., Phillips, A. C., Kibrick, R. I., et al. 2003, in *Society of Photo-Optical Instrumentation Engineers (SPIE) Conference Series*, Vol. 4841, *Instrument Design and Performance for Optical/Infrared Ground-based Telescopes*, ed. M. Iye & A. F. M. Moorwood, 1657–1669, doi: [10.1117/12.460346](https://doi.org/10.1117/12.460346)
- Feroz, F., & Hobson, M. P. 2008, *MNRAS*, 384, 449, doi: [10.1111/j.1365-2966.2007.12353.x](https://doi.org/10.1111/j.1365-2966.2007.12353.x)
- Feroz, F., Hobson, M. P., & Bridges, M. 2009, *MNRAS*, 398, 1601, doi: [10.1111/j.1365-2966.2009.14548.x](https://doi.org/10.1111/j.1365-2966.2009.14548.x)
- Feroz, F., Hobson, M. P., Cameron, E., & Pettitt, A. N. 2019, *The Open Journal of Astrophysics*, 2, 10, doi: [10.21105/astro.1306.2144](https://doi.org/10.21105/astro.1306.2144)
- Fitzpatrick, E. L. 1999, *PASP*, 111, 63, doi: [10.1086/316293](https://doi.org/10.1086/316293)
- Flewelling, H. A., Magnier, E. A., Chambers, K. C., et al. 2020, *ApJS*, 251, 7, doi: [10.3847/1538-4365/abb82d](https://doi.org/10.3847/1538-4365/abb82d)
- Foreman-Mackey, D., Luger, R., Agol, E., et al. 2021a, *The Journal of Open Source Software*, 6, 3285, doi: [10.21105/joss.03285](https://doi.org/10.21105/joss.03285)
- . 2021b, exoplanet: Gradient-based probabilistic inference for exoplanet data & other astronomical time series, 0.5.1, Zenodo, Zenodo, doi: [10.5281/zenodo.1998447](https://doi.org/10.5281/zenodo.1998447)
- Frost, A. J., Bodensteiner, J., Rivinius, T., et al. 2022, *A&A*, 659, L3, doi: [10.1051/0004-6361/202143004](https://doi.org/10.1051/0004-6361/202143004)
- Fukugita, M., Ichikawa, T., Gunn, J. E., et al. 1996, *AJ*, 111, 1748, doi: [10.1086/117915](https://doi.org/10.1086/117915)
- Fulton, B. J., Weiss, L. M., Sinukoff, E., et al. 2015, *ApJ*, 805, 175, doi: [10.1088/0004-637X/805/2/175](https://doi.org/10.1088/0004-637X/805/2/175)
- Gaia Collaboration, Prusti, T., de Bruijne, J. H. J., et al. 2016, *A&A*, 595, A1, doi: [10.1051/0004-6361/201629272](https://doi.org/10.1051/0004-6361/201629272)
- Gaia Collaboration, Arenou, F., Babusiaux, C., et al. 2022a, arXiv e-prints, arXiv:2206.05595. <https://arxiv.org/abs/2206.05595>
- Gaia Collaboration, Vallenari, A., Brown, A. G. A., et al. 2022b, arXiv e-prints, arXiv:2208.00211. <https://arxiv.org/abs/2208.00211>
- Gao, S., Liu, C., Zhang, X., et al. 2014, *ApJL*, 788, L37, doi: [10.1088/2041-8205/788/2/L37](https://doi.org/10.1088/2041-8205/788/2/L37)
- Giesers, B., Dreizler, S., Husser, T.-O., et al. 2018, *MNRAS*, 475, L15, doi: [10.1093/mnrasl/slx203](https://doi.org/10.1093/mnrasl/slx203)
- Giesers, B., Kamann, S., Dreizler, S., et al. 2019, *A&A*, 632, A3, doi: [10.1051/0004-6361/201936203](https://doi.org/10.1051/0004-6361/201936203)
- Gilkis, A., Shenar, T., Ramachandran, V., et al. 2021, *MNRAS*, 503, 1884, doi: [10.1093/mnras/stab383](https://doi.org/10.1093/mnras/stab383)
- González Hernández, J. I., Rebolo, R., Israelian, G., et al. 2008, *ApJ*, 679, 732, doi: [10.1086/586888](https://doi.org/10.1086/586888)
- GRAVITY Collaboration, Karl, M., Pfuhl, O., et al. 2018, *A&A*, 620, A116, doi: [10.1051/0004-6361/201833575](https://doi.org/10.1051/0004-6361/201833575)

- Gray, R. O., Corbally, C. J., Garrison, R. F., McFadden, M. T., & Robinson, P. E. 2003, *AJ*, 126, 2048, doi: [10.1086/378365](https://doi.org/10.1086/378365)
- Gray, R. O., & Corbally, Christopher, J. 2009, *Stellar Spectral Classification*
- Halbwachs, J.-L., Pourbaix, D., Arenou, F., et al. 2022, arXiv e-prints, arXiv:2206.05726, <https://arxiv.org/abs/2206.05726>
- Henden, A. A. 2019, *JAAVSO*, 47, 130
- Henden, A. A., Templeton, M., Terrell, D., et al. 2016, *VizieR Online Data Catalog*, II/336
- Holl, B., Sozzetti, A., Sahlmann, J., et al. 2022, arXiv e-prints, arXiv:2206.05439, <https://arxiv.org/abs/2206.05439>
- Howard, A. W., Johnson, J. A., Marcy, G. W., et al. 2010, *ApJ*, 721, 1467, doi: [10.1088/0004-637X/721/2/1467](https://doi.org/10.1088/0004-637X/721/2/1467)
- Husser, T. O., Wende-von Berg, S., Dreizler, S., et al. 2013, *A&A*, 553, A6, doi: [10.1051/0004-6361/201219058](https://doi.org/10.1051/0004-6361/201219058)
- Janssens, S., Shenar, T., Sana, H., et al. 2022, *A&A*, 658, A129, doi: [10.1051/0004-6361/202141866](https://doi.org/10.1051/0004-6361/202141866)
- Jayasinghe, T., Stanek, K. Z., Thompson, T. A., et al. 2021, *MNRAS*, 504, 2577, doi: [10.1093/mnras/stab907](https://doi.org/10.1093/mnras/stab907)
- Jayasinghe, T., Thompson, T. A., Kochanek, C. S., et al. 2022, *MNRAS*, doi: [10.1093/mnras/stac2187](https://doi.org/10.1093/mnras/stac2187)
- Ji, A. P., Li, T. S., Simon, J. D., et al. 2020, *ApJ*, 889, 27, doi: [10.3847/1538-4357/ab6213](https://doi.org/10.3847/1538-4357/ab6213)
- Kelson, D. D. 2003, *PASP*, 115, 688, doi: [10.1086/375502](https://doi.org/10.1086/375502)
- Kennicutt, Robert C., J., Bresolin, F., & Garnett, D. R. 2003, *ApJ*, 591, 801, doi: [10.1086/375398](https://doi.org/10.1086/375398)
- Kirby, E. N., Simon, J. D., & Cohen, J. G. 2015, *ApJ*, 810, 56, doi: [10.1088/0004-637X/810/1/56](https://doi.org/10.1088/0004-637X/810/1/56)
- Kobayashi, C., Karakas, A. I., & Lugaro, M. 2020, *ApJ*, 900, 179, doi: [10.3847/1538-4357/abae65](https://doi.org/10.3847/1538-4357/abae65)
- Lallement, R., Vergely, J. L., Valette, B., et al. 2014, *A&A*, 561, A91, doi: [10.1051/0004-6361/201322032](https://doi.org/10.1051/0004-6361/201322032)
- Lallement, R., Capitano, L., Ruiz-Dern, L., et al. 2018, *A&A*, 616, A132, doi: [10.1051/0004-6361/201832832](https://doi.org/10.1051/0004-6361/201832832)
- Lam, C. Y., Lu, J. R., Udalski, A., et al. 2022, *ApJL*, 933, L23, doi: [10.3847/2041-8213/ac7442](https://doi.org/10.3847/2041-8213/ac7442)
- Lamberts, A., Garrison-Kimmel, S., Clausen, D. R., & Hopkins, P. F. 2016, *MNRAS*, 463, L31, doi: [10.1093/mnras/463/l31](https://doi.org/10.1093/mnras/463/l31)
- Lehmer, B. D., Eufrazio, R. T., Basu-Zych, A., et al. 2021, *ApJ*, 907, 17, doi: [10.3847/1538-4357/abcec1](https://doi.org/10.3847/1538-4357/abcec1)
- Lejeune, T., Cuisinier, F., & Buser, R. 1997, *A&AS*, 125, 229, doi: [10.1051/aas:1997373](https://doi.org/10.1051/aas:1997373)
- . 1998, *A&AS*, 130, 65, doi: [10.1051/aas:1998405](https://doi.org/10.1051/aas:1998405)
- Lennon, D. J., Dufton, P. L., Villaseñor, J. I., et al. 2021, arXiv e-prints, arXiv:2111.12173, <https://arxiv.org/abs/2111.12173>
- . 2022, *A&A*, 665, A180, doi: [10.1051/0004-6361/202142413](https://doi.org/10.1051/0004-6361/202142413)
- Lind, K., Asplund, M., Barklem, P. S., & Belyaev, A. K. 2011, *A&A*, 528, A103, doi: [10.1051/0004-6361/201016095](https://doi.org/10.1051/0004-6361/201016095)
- Lindegren, L., Klioner, S. A., Hernández, J., et al. 2021a, *A&A*, 649, A2, doi: [10.1051/0004-6361/202039709](https://doi.org/10.1051/0004-6361/202039709)
- Lindegren, L., Bastian, U., Biermann, M., et al. 2021b, *A&A*, 649, A4, doi: [10.1051/0004-6361/202039653](https://doi.org/10.1051/0004-6361/202039653)
- Lipartito, I., Bailey, John I., I., Brandt, T. D., et al. 2021, *AJ*, 162, 285, doi: [10.3847/1538-3881/ac2ccd](https://doi.org/10.3847/1538-3881/ac2ccd)
- Liu, J., Zhang, H., Howard, A. W., et al. 2019, *Nature*, 575, 618, doi: [10.1038/s41586-019-1766-2](https://doi.org/10.1038/s41586-019-1766-2)
- Luo, A. L., Zhao, Y. H., Zhao, G., & et al. 2022, *VizieR Online Data Catalog*, V/156
- Mahy, L., Sana, H., Shenar, T., et al. 2022, *A&A*, 664, A159, doi: [10.1051/0004-6361/202243147](https://doi.org/10.1051/0004-6361/202243147)
- Maíz Apellániz, J., Sota, A., Arias, J. I., et al. 2016, *ApJS*, 224, 4, doi: [10.3847/0067-0049/224/1/4](https://doi.org/10.3847/0067-0049/224/1/4)
- Marchant, P., Pappas, K. M. W., Gallegos-Garcia, M., et al. 2021, *A&A*, 650, A107, doi: [10.1051/0004-6361/202039992](https://doi.org/10.1051/0004-6361/202039992)
- Martin, D. C., Fanson, J., Schiminovich, D., et al. 2005, *ApJL*, 619, L1, doi: [10.1086/426387](https://doi.org/10.1086/426387)
- Martins, F., & Palacios, A. 2013, *A&A*, 560, A16, doi: [10.1051/0004-6361/201322480](https://doi.org/10.1051/0004-6361/201322480)
- Mashian, N., & Loeb, A. 2017, *MNRAS*, 470, 2611, doi: [10.1093/mnras/stx1410](https://doi.org/10.1093/mnras/stx1410)
- McWilliam, A. 1998, *AJ*, 115, 1640, doi: [10.1086/300289](https://doi.org/10.1086/300289)
- Meléndez, J., Schirbel, L., Monroe, T. R., et al. 2014, *A&A*, 567, L3, doi: [10.1051/0004-6361/201424172](https://doi.org/10.1051/0004-6361/201424172)
- Mirabel, I. F., & Rodrigues, I. 2003, *Science*, 300, 1119, doi: [10.1126/science.1083451](https://doi.org/10.1126/science.1083451)
- Moe, M., Kratter, K. M., & Badenes, C. 2019, *ApJ*, 875, 61, doi: [10.3847/1538-4357/ab0d88](https://doi.org/10.3847/1538-4357/ab0d88)
- Morrissey, P., Conrow, T., Barlow, T. A., et al. 2007, *ApJS*, 173, 682, doi: [10.1086/520512](https://doi.org/10.1086/520512)
- Morton, T. D. 2015, *isochrones: Stellar model grid package*. <http://ascl.net/1503.010>
- Naoz, S., Farr, W. M., Lithwick, Y., Rasio, F. A., & Teyssandier, J. 2013, *MNRAS*, 431, 2155, doi: [10.1093/mnras/stt302](https://doi.org/10.1093/mnras/stt302)
- Neijssel, C. J., Vigna-Gómez, A., Stevenson, S., et al. 2019, *MNRAS*, 490, 3740, doi: [10.1093/mnras/stz2840](https://doi.org/10.1093/mnras/stz2840)
- Newman, J. A., Cooper, M. C., Davis, M., et al. 2013, *ApJS*, 208, 5, doi: [10.1088/0067-0049/208/1/5](https://doi.org/10.1088/0067-0049/208/1/5)
- Olejak, A., Belczynski, K., Bulik, T., & Sobolewska, M. 2020, *A&A*, 638, A94, doi: [10.1051/0004-6361/201936557](https://doi.org/10.1051/0004-6361/201936557)
- Onken, C. A., Wolf, C., Bessell, M. S., et al. 2019, *PASA*, 36, e033, doi: [10.1017/pasa.2019.27](https://doi.org/10.1017/pasa.2019.27)

- Orosz, J. A., Kuulkers, E., van der Klis, M., et al. 2001, *ApJ*, 555, 489, doi: [10.1086/321442](https://doi.org/10.1086/321442)
- Özel, F., Psaltis, D., Narayan, R., & McClintock, J. E. 2010, *ApJ*, 725, 1918, doi: [10.1088/0004-637X/725/2/1918](https://doi.org/10.1088/0004-637X/725/2/1918)
- Panizo-Espinar, G., Armas Padilla, M., Muñoz-Darias, T., et al. 2022, *A&A*, 664, A100, doi: [10.1051/0004-6361/202243426](https://doi.org/10.1051/0004-6361/202243426)
- Paxton, B., Bildsten, L., Dotter, A., et al. 2011, *ApJS*, 192, 3, doi: [10.1088/0067-0049/192/1/3](https://doi.org/10.1088/0067-0049/192/1/3)
- Paxton, B., Smolec, R., Schwab, J., et al. 2019, *ApJS*, 243, 10, doi: [10.3847/1538-4365/ab2241](https://doi.org/10.3847/1538-4365/ab2241)
- Pinsonneault, M. H., Elsworth, Y. P., Tayar, J., et al. 2018, *ApJS*, 239, 32, doi: [10.3847/1538-4365/aaebfd](https://doi.org/10.3847/1538-4365/aaebfd)
- Price-Whelan, A. M., Hogg, D. W., Foreman-Mackey, D., & Rix, H.-W. 2017, *ApJ*, 837, 20, doi: [10.3847/1538-4357/aa5e50](https://doi.org/10.3847/1538-4357/aa5e50)
- Prochaska, J. X., & McWilliam, A. 2000, *ApJL*, 537, L57, doi: [10.1086/312749](https://doi.org/10.1086/312749)
- Prochaska, J. X., Naumov, S. O., Carney, B. W., McWilliam, A., & Wolfe, A. M. 2000, *AJ*, 120, 2513, doi: [10.1086/316818](https://doi.org/10.1086/316818)
- Radovan, M. V., Cabak, G. F., Laiterman, L. H., Lockwood, C. T., & Vogt, S. S. 2010, in *Society of Photo-Optical Instrumentation Engineers (SPIE) Conference Series*, Vol. 7735, *Ground-based and Airborne Instrumentation for Astronomy III*, ed. I. S. McLean, S. K. Ramsay, & H. Takami, 77354K, doi: [10.1117/12.857726](https://doi.org/10.1117/12.857726)
- Raithel, C. A., Sukhbold, T., & Özel, F. 2018, *ApJ*, 856, 35, doi: [10.3847/1538-4357/aab09b](https://doi.org/10.3847/1538-4357/aab09b)
- Ramachandran, V., Hamann, W. R., Oskinova, L. M., et al. 2019, *A&A*, 625, A104, doi: [10.1051/0004-6361/201935365](https://doi.org/10.1051/0004-6361/201935365)
- Reggiani, H., Ji, A. P., Schlaufman, K. C., et al. 2022a, *AJ*, 163, 252, doi: [10.3847/1538-3881/ac62d9](https://doi.org/10.3847/1538-3881/ac62d9)
- Reggiani, H., & Meléndez, J. 2018, *MNRAS*, 475, 3502, doi: [10.1093/mnras/sty104](https://doi.org/10.1093/mnras/sty104)
- Reggiani, H., Schlaufman, K. C., Healy, B. F., Lothringer, J. D., & Sing, D. K. 2022b, *AJ*, 163, 159, doi: [10.3847/1538-3881/ac4d9f](https://doi.org/10.3847/1538-3881/ac4d9f)
- Reggiani, H., Amarsi, A. M., Lind, K., et al. 2019, *A&A*, 627, A177, doi: [10.1051/0004-6361/201935156](https://doi.org/10.1051/0004-6361/201935156)
- Reggiani, M., Rainot, A., Sana, H., et al. 2022c, *A&A*, 660, A122, doi: [10.1051/0004-6361/202142418](https://doi.org/10.1051/0004-6361/202142418)
- Riello, M., De Angeli, F., Evans, D. W., et al. 2021, *A&A*, 649, A3, doi: [10.1051/0004-6361/202039587](https://doi.org/10.1051/0004-6361/202039587)
- Rivinius, T., Baade, D., Hadrava, P., Heida, M., & Klement, R. 2020, *A&A*, 637, L3, doi: [10.1051/0004-6361/202038020](https://doi.org/10.1051/0004-6361/202038020)
- Russell, T. D., Del Santo, M., Marino, A., et al. 2022, *MNRAS*, 513, 6196, doi: [10.1093/mnras/stac1332](https://doi.org/10.1093/mnras/stac1332)
- Sahu, K. C., Anderson, J., Casertano, S., et al. 2022, *ApJ*, 933, 83, doi: [10.3847/1538-4357/ac739e](https://doi.org/10.3847/1538-4357/ac739e)
- Sana, H., Gosset, E., & Evans, C. J. 2009, *MNRAS*, 400, 1479, doi: [10.1111/j.1365-2966.2009.15545.x](https://doi.org/10.1111/j.1365-2966.2009.15545.x)
- Sana, H., de Mink, S. E., de Koter, A., et al. 2012, *Science*, 337, 444, doi: [10.1126/science.1223344](https://doi.org/10.1126/science.1223344)
- Saracino, S., Kamann, S., Guarcello, M. G., et al. 2022, *MNRAS*, 511, 2914, doi: [10.1093/mnras/stab3159](https://doi.org/10.1093/mnras/stab3159)
- Shahaf, S., Bashi, D., Mazeh, T., et al. 2022, *arXiv e-prints*, arXiv:2209.00828. <https://arxiv.org/abs/2209.00828>
- Shao, Y., & Li, X.-D. 2019, *ApJ*, 885, 151, doi: [10.3847/1538-4357/ab4816](https://doi.org/10.3847/1538-4357/ab4816)
- Shenar, T., Bodensteiner, J., Abdul-Masih, M., et al. 2020, *A&A*, 639, L6, doi: [10.1051/0004-6361/202038275](https://doi.org/10.1051/0004-6361/202038275)
- Shenar, T., Sana, H., Mahy, L., et al. 2022, *Nature Astronomy*, 6, 1085, doi: [10.1038/s41550-022-01730-y](https://doi.org/10.1038/s41550-022-01730-y)
- Shikauchi, M., Tanikawa, A., & Kawanaka, N. 2022, *ApJ*, 928, 13, doi: [10.3847/1538-4357/ac5329](https://doi.org/10.3847/1538-4357/ac5329)
- Simon, J. D., & Geha, M. 2007, *ApJ*, 670, 313, doi: [10.1086/521816](https://doi.org/10.1086/521816)
- Simon, J. D., Li, T. S., Drlica-Wagner, A., et al. 2017, *ApJ*, 838, 11, doi: [10.3847/1538-4357/aa5be7](https://doi.org/10.3847/1538-4357/aa5be7)
- Skrutskie, M. F., Cutri, R. M., Stiening, R., et al. 2006, *AJ*, 131, 1163, doi: [10.1086/498708](https://doi.org/10.1086/498708)
- Snedden, C. A. 1973, PhD thesis, THE UNIVERSITY OF TEXAS AT AUSTIN.
- Sohn, S. T., Majewski, S. R., Muñoz, R. R., et al. 2007, *ApJ*, 663, 960, doi: [10.1086/518302](https://doi.org/10.1086/518302)
- Soubiran, C., Jasniewicz, G., Chemin, L., et al. 2018, *A&A*, 616, A7, doi: [10.1051/0004-6361/201832795](https://doi.org/10.1051/0004-6361/201832795)
- Stefanik, R. P., Latham, D. W., & Torres, G. 1999, in *Astronomical Society of the Pacific Conference Series*, Vol. 185, *IAU Colloq. 170: Precise Stellar Radial Velocities*, ed. J. B. Hearnshaw & C. D. Scarfe, 354
- Suárez-Andrés, L., González Hernández, J. I., Israelian, G., Casares, J., & Rebolo, R. 2015, *MNRAS*, 447, 2261, doi: [10.1093/mnras/stu2612](https://doi.org/10.1093/mnras/stu2612)
- Sukhbold, T., Ertl, T., Woosley, S. E., Brown, J. M., & Janka, H. T. 2016, *ApJ*, 821, 38, doi: [10.3847/0004-637X/821/1/38](https://doi.org/10.3847/0004-637X/821/1/38)
- Suzuki, H., Gupta, P., Okawa, H., & Maeda, K.-i. 2019, *MNRAS*, 486, L52, doi: [10.1093/mnrasl/slz058](https://doi.org/10.1093/mnrasl/slz058)
- Tanikawa, A., Hattori, K., Kawanaka, N., et al. 2022, *arXiv e-prints*, arXiv:2209.05632, doi: [10.48550/arXiv.2209.05632](https://doi.org/10.48550/arXiv.2209.05632)
- Thompson, T. A., Kochanek, C. S., Stanek, K. Z., et al. 2019, *Science*, 366, 637, doi: [10.1126/science.aau4005](https://doi.org/10.1126/science.aau4005)

- Tokovinin, A., & Moe, M. 2020, MNRAS, 491, 5158, doi: [10.1093/mnras/stz3299](https://doi.org/10.1093/mnras/stz3299)
- Tokovinin, A., Thomas, S., Sterzik, M., & Udry, S. 2006, A&A, 450, 681, doi: [10.1051/0004-6361:20054427](https://doi.org/10.1051/0004-6361:20054427)
- Tonry, J. L., Stubbs, C. W., Lykke, K. R., et al. 2012, ApJ, 750, 99, doi: [10.1088/0004-637X/750/2/99](https://doi.org/10.1088/0004-637X/750/2/99)
- van den Heuvel, E. P. J., Portegies Zwart, S. F., & de Mink, S. E. 2017, MNRAS, 471, 4256, doi: [10.1093/mnras/stx1430](https://doi.org/10.1093/mnras/stx1430)
- van den Heuvel, E. P. J., & Tauris, T. M. 2020a, Science, 368, eaba3282, doi: [10.1126/science.aba3282](https://doi.org/10.1126/science.aba3282)
- . 2020b, Science, 368, eaba3282, doi: [10.1126/science.aba3282](https://doi.org/10.1126/science.aba3282)
- Vigna-Gómez, A., Liu, B., Aguilera-Dena, D. R., et al. 2022, MNRAS, 515, L50, doi: [10.1093/mnrasl/slac067](https://doi.org/10.1093/mnrasl/slac067)
- Vines, J. I., & Jenkins, J. S. 2022, MNRAS, 513, 2719, doi: [10.1093/mnras/stac956](https://doi.org/10.1093/mnras/stac956)
- Vogt, S. S., Radovan, M., Kibrick, R., et al. 2014, PASP, 126, 359, doi: [10.1086/676120](https://doi.org/10.1086/676120)
- Wang, Y., Liao, S., Giacobbo, N., et al. 2022, A&A, 665, A111, doi: [10.1051/0004-6361/202243684](https://doi.org/10.1051/0004-6361/202243684)
- Wiktorowicz, G., Lu, Y., Wyrzykowski, L., et al. 2020, ApJ, 905, 134, doi: [10.3847/1538-4357/abc699](https://doi.org/10.3847/1538-4357/abc699)
- Wiktorowicz, G., Wyrzykowski, L., Chruslinska, M., et al. 2019, ApJ, 885, 1, doi: [10.3847/1538-4357/ab45e6](https://doi.org/10.3847/1538-4357/ab45e6)
- Wolf, C., Onken, C. A., Luvaul, L. C., et al. 2018, PASA, 35, e010, doi: [10.1017/pasa.2018.5](https://doi.org/10.1017/pasa.2018.5)
- Wright, E. L., Eisenhardt, P. R. M., Mainzer, A. K., et al. 2010, AJ, 140, 1868, doi: [10.1088/0004-6256/140/6/1868](https://doi.org/10.1088/0004-6256/140/6/1868)
- Wright, J. T. 2005, PASP, 117, 657, doi: [10.1086/430369](https://doi.org/10.1086/430369)
- Yalinewich, A., Beniamini, P., Hotokezaka, K., & Zhu, W. 2018, MNRAS, 481, 930, doi: [10.1093/mnras/sty2327](https://doi.org/10.1093/mnras/sty2327)
- Yamaguchi, M. S., Kawanaka, N., Bulik, T., & Piran, T. 2018, ApJ, 861, 21, doi: [10.3847/1538-4357/aac5ec](https://doi.org/10.3847/1538-4357/aac5ec)
- Yee, S. W., Petigura, E. A., & von Braun, K. 2017, ApJ, 836, 77, doi: [10.3847/1538-4357/836/1/77](https://doi.org/10.3847/1538-4357/836/1/77)

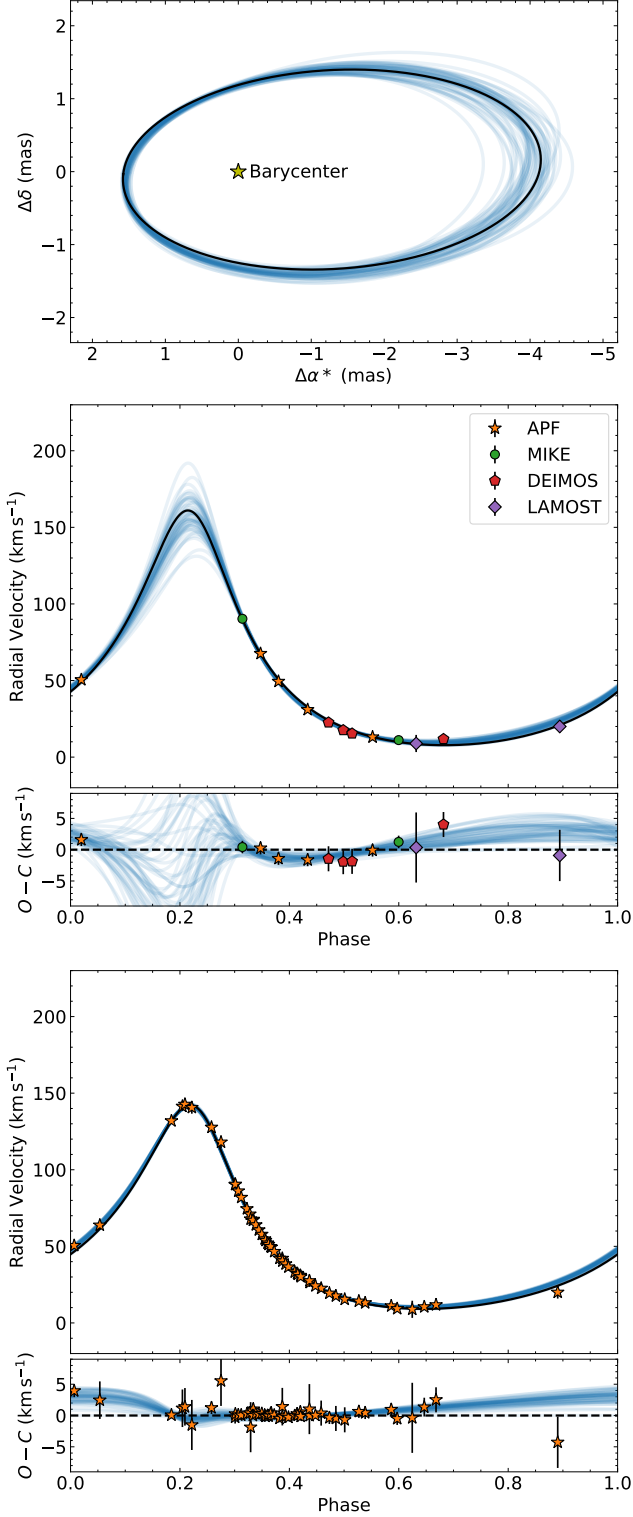


Figure 14. Joint orbital fit (see text for the description of the joint fit)

to the astrometry (top) and radial velocities (middle) for the RV data set given in Table 2, and for all available radial velocity data (bottom). The black lines in the lower two panels show the steps in the RV chains most consistent with the Gaia astrometry; these orbits are in tension with the RVs. The light blue points are drawn from weighted RV chains conditioned on the Gaia data as described in the text.

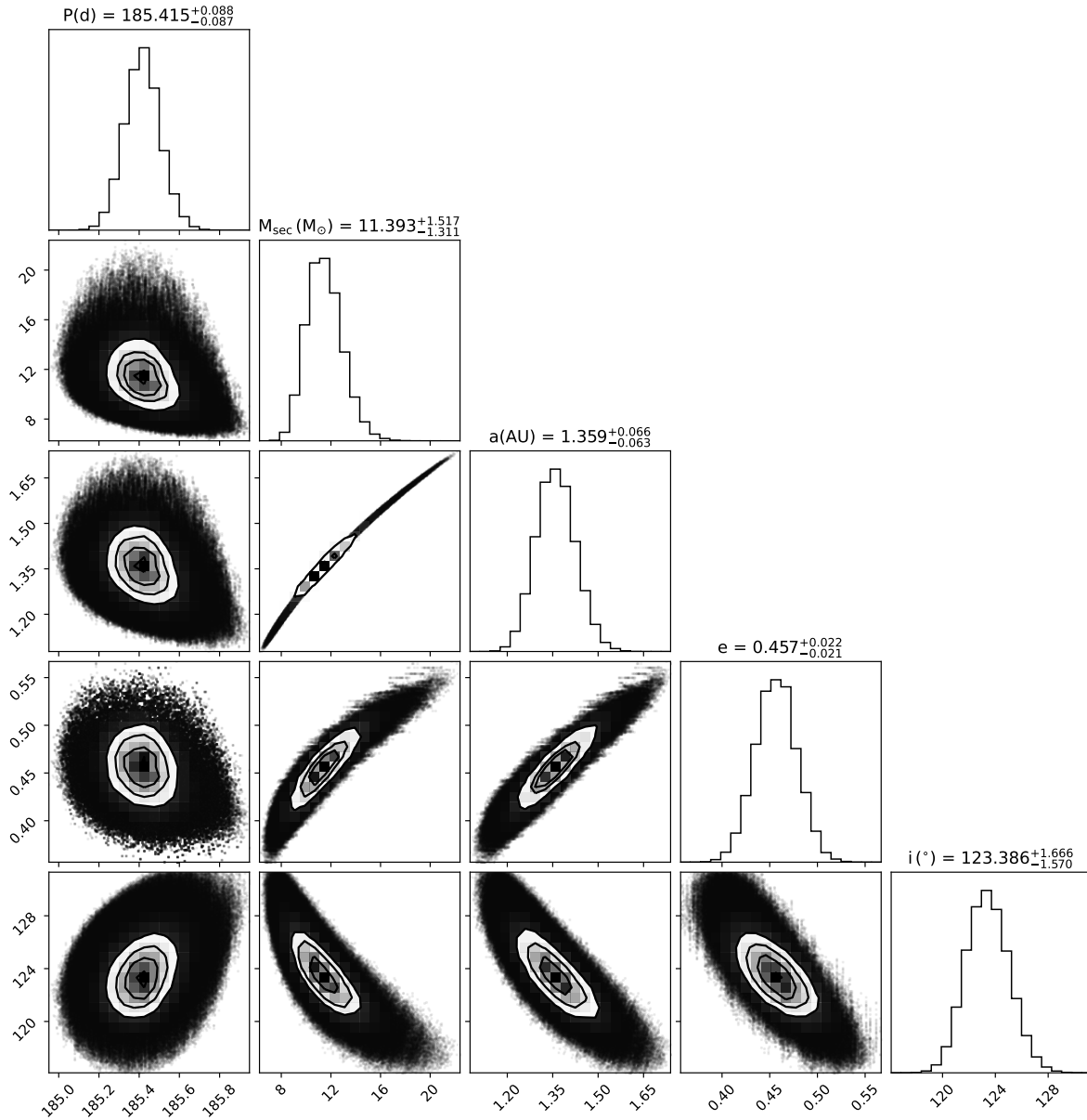


Figure 15. Posterior distributions from our joints fits to our velocity data and LAMOST data (as listed in Table 2), and *Gaia* astrometry. The parameter constraints are tighter and correlations are reduced compared to the fit to the velocities alone.

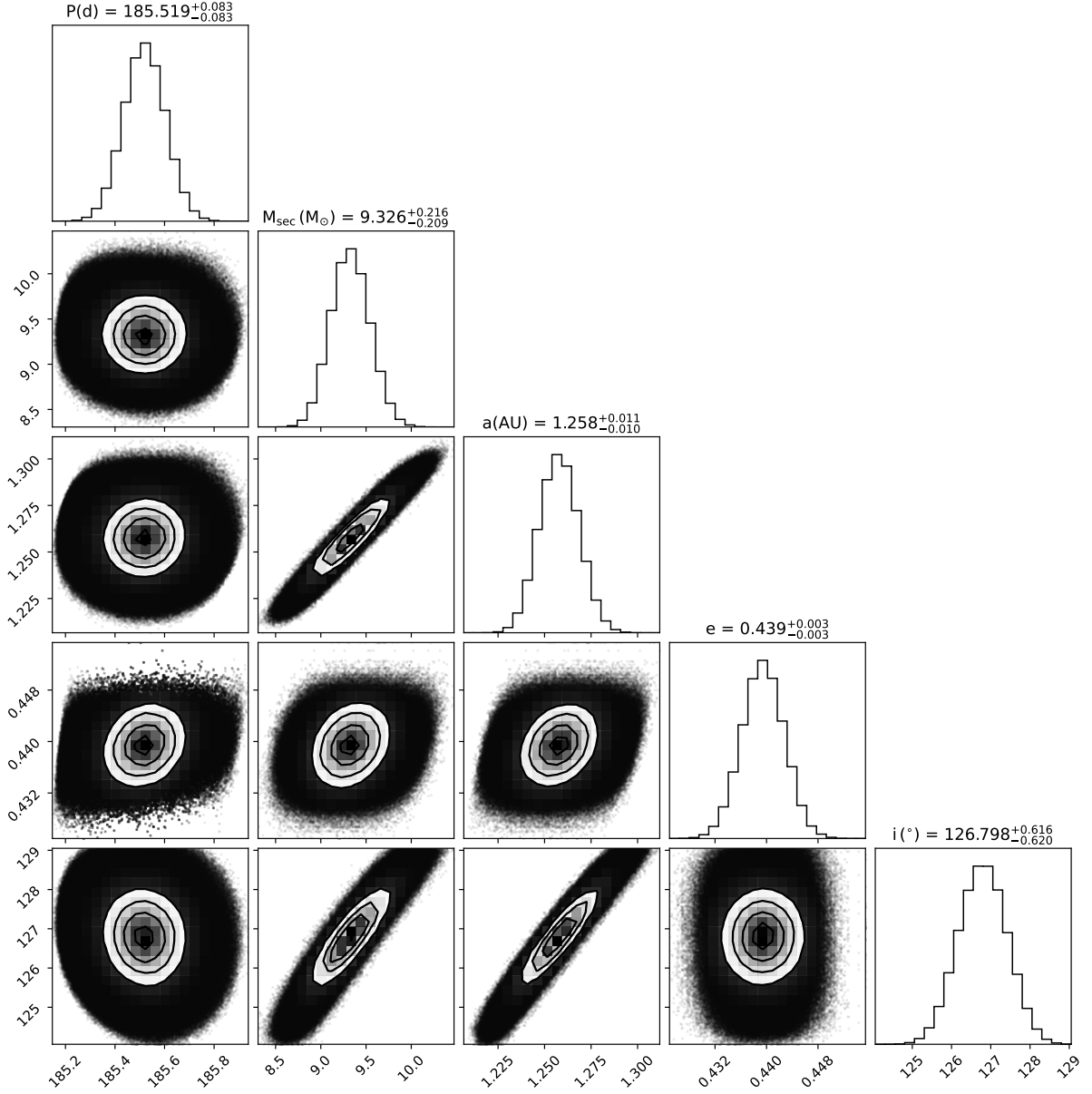


Figure 16. Posterior distributions from our joint fits to all available velocity data (including RV data from El-Badry et al. 2023) and *Gaia* astrometry. The parameter constraints are tighter and correlations are reduced compared to the fit to the velocities alone.

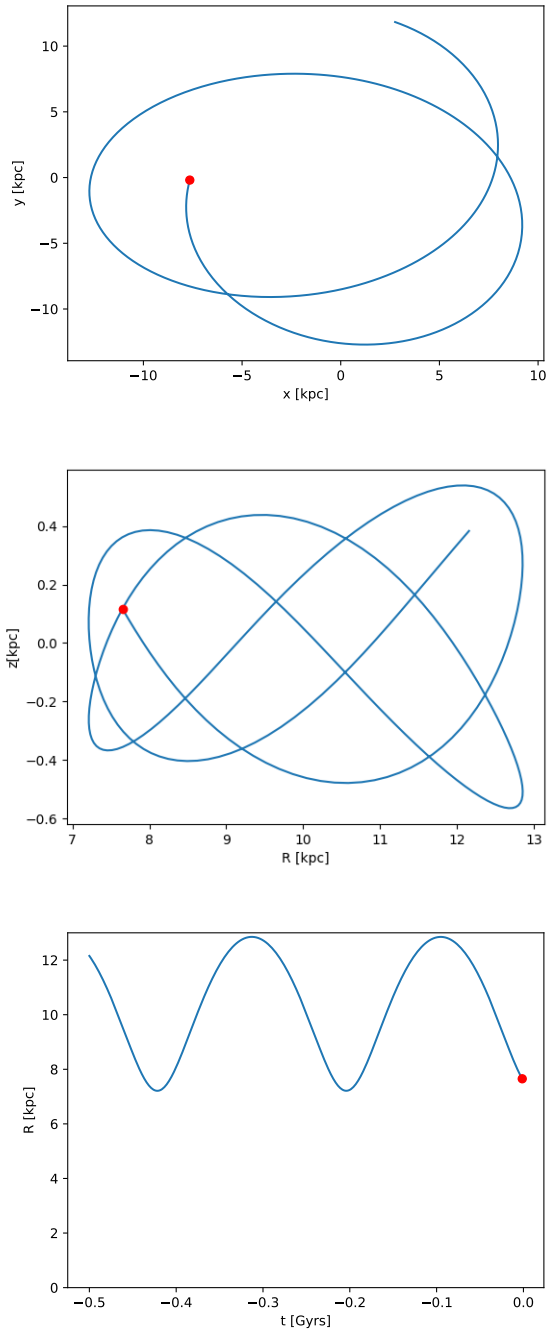


Figure 17. Orbit in the Galaxy, integrated backwards from present day for 500 Myr; the red dot marks the present day ($t = 0$).